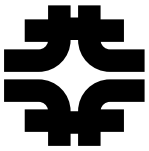

Fermi National Accelerator Laboratory

FERMILAB-Pub-98/392-E
CDF

Measurement of $b\bar{b}$ Rapidity Correlations in $p\bar{p}$ Collisions at $\sqrt{s}$ = 1.8 TeV

F. Abe et al.
The CDF Collaboration

Fermi National Accelerator Laboratory
P.O. Box 500, Batavia, Illinois 60510

January 1999

Submitted to *Physical Review D*

Operated by Universities Research Association Inc. under Contract No. DE-AC02-76CH03000 with the United States Department of Energy

Measurement of $b\bar{b}$ Rapidity Correlations in $p\bar{p}$ Collisions at $\sqrt{s} = 1.8\,\mathrm{TeV}$

F. Abe,[17] H. Akimoto,[39] A. Akopian,[31] M. G. Albrow,[7] A. Amadon,[5] S. R. Amendolia,[27] D. Amidei,[20] J. Antos,[33] S. Aota,[37] G. Apollinari,[31] T. Arisawa,[39] T. Asakawa,[37] W. Ashmanskas,[5] M. Atac,[7] P. Azzi-Bacchetta,[25] N. Bacchetta,[25] S. Bagdasarov,[31] M. W. Bailey,[22] P. de Barbaro,[30] A. Barbaro-Galtieri,[18] V. E. Barnes,[29] B. A. Barnett,[15] M. Barone,[9] G. Bauer,[19] T. Baumann,[11] F. Bedeschi,[27] S. Behrends,[3] S. Belforte,[27] G. Bellettini,[27] J. Bellinger,[40] D. Benjamin,[35] J. Bensinger,[3] A. Beretvas,[7] J. P. Berge,[7] J. Berryhill,[5] S. Bertolucci,[9] S. Bettelli,[27] B. Bevensee,[26] A. Bhatti,[31] K. Biery,[7] C. Bigongiari,[27] M. Binkley,[7] D. Bisello,[25] R. E. Blair,[1] C. Blocker,[3] K. Bloom,[20] S. Blusk,[30] A. Bodek,[30] W. Bokhari,[26] G. Bolla,[29] Y. Bonushkin,[4] D. Bortoletto,[29] J. Boudreau,[28] L. Breccia,[2] C. Bromberg,[21] N. Bruner,[22] R. Brunetti,[2] E. Buckley-Geer,[7] H. S. Budd,[30] K. Burkett,[11] G. Busetto,[25] A. Byon-Wagner,[7] K. L. Byrum,[1] M. Campbell,[20] A. Caner,[27] W. Carithers,[18] D. Carlsmith,[40] J. Cassada,[30] A. Castro,[25] D. Cauz,[36] A. Cerri,[27] P. S. Chang,[33] P. T. Chang,[33] H. Y. Chao,[33] J. Chapman,[20] M. -T. Cheng,[33] M. Chertok,[34] G. Chiarelli,[27] C. N. Chiou,[33] F. Chlebana,[7] L. Christofek,[13] R. Cropp,[14] M. L. Chu,[33] S. Cihangir,[7] A. G. Clark,[10] M. Cobal,[27] E. Cocca,[27] M. Contreras,[5] J. Conway,[32] J. Cooper,[7] M. Cordelli,[9] D. Costanzo,[27] C. Couyoumtzelis,[10] D. Cronin-Hennessy,[6] R. Culbertson,[5] D. Dagenhart,[38] T. Daniels,[19] F. DeJongh,[7] S. Dell'Agnello,[9] M. Dell'Orso,[27] R. Demina,[7] L. Demortier,[31] M. Deninno,[2] P. F. Derwent,[7] T. Devlin,[32] J. R. Dittmann,[6] S. Donati,[27] J. Done,[34] T. Dorigo,[25] N. Eddy,[13] K. Einsweiler,[18] J. E. Elias,[7] R. Ely,[18] E. Engels, Jr.,[28] W. Erdmann,[7] D. Errede,[13] S. Errede,[13] Q. Fan,[30] R. G. Feild,[41] Z. Feng,[15] C. Ferretti,[27] I. Fiori,[2] B. Flaugher,[7] G. W. Foster,[7] M. Franklin,[11] J. Freeman,[7] J. Friedman,[19] Y. Fukui,[17] S. Gadomski,[14] S. Galeotti,[27] M. Gallinaro,[26] O. Ganel,[35] M. Garcia-Sciveres,[18] A. F. Garfinkel,[29] C. Gay,[41] S. Geer,[7] D. W. Gerdes,[20] P. Giannetti,[27] N. Giokaris,[31] P. Giromini,[9] G. Giusti,[27] M. Gold,[22] A. Gordon,[11] A. T. Goshaw,[6] Y. Gotra,[28] K. Goulianos,[31] H. Grassmann,[36] C. Green,[29] L. Groer,[32] C. Grosso-Pilcher,[5] G. Guillian,[20] J. Guimaraes da Costa,[15] R. S. Guo,[33] C. Haber,[18] E. Hafen,[19] S. R. Hahn,[7] R. Hamilton,[11] T. Handa,[12] R. Handler,[40] W. Hao,[35] F. Happacher,[9] K. Hara,[37] A. D. Hardman,[29] R. M. Harris,[7] F. Hartmann,[16] J. Hauser,[4] E. Hayashi,[37] J. Heinrich,[26] A. Heiss,[16] B. Hinrichsen,[14] K. D. Hoffman,[29] C. Holck,[26] R. Hollebeek,[26] L. Holloway,[13] Z. Huang,[20] B. T. Huffman,[28] R. Hughes,[23] J. Huston,[21] J. Huth,[11] H. Ikeda,[37] M. Incagli,[27] J. Incandela,[7] G. Introzzi,[27] J. Iwai,[39] Y. Iwata,[12] E. James,[20] H. Jensen,[7] U. Joshi,[7] E. Kajfasz,[25] H. Kambara,[10] T. Kamon,[34] T. Kaneko,[37] K. Karr,[38] H. Kasha,[41] Y. Kato,[24] T. A. Keaffaber,[29] K. Kelley,[19] R. D. Kennedy,[7] R. Kephart,[7] D. Kestenbaum,[11] D. Khazins,[6] T. Kikuchi,[37] B. J. Kim,[27] H. S. Kim,[14] S. H. Kim,[37] Y. K. Kim,[18] L. Kirsch,[3] S. Klimenko,[8] D. Knoblauch,[16] P. Koehn,[23] A. Köngeter,[16] K. Kondo,[37] J. Konigsberg,[8] K. Kordas,[14] A. Korytov,[8] E. Kovacs,[1] W. Kowald,[6] J. Kroll,[26] M. Kruse,[30] S. E. Kuhlmann,[1] E. Kuns,[32] K. Kurino,[12] T. Kuwabara,[37] A. T. Laasanen,[29] S. Lami,[27] S. Lammel,[7] J. I. Lamoureux,[3] M. Lancaster,[18] M. Lanzoni,[27] G. Latino,[27] T. LeCompte,[1] S. Leone,[27] J. D. Lewis,[7] M. Lindgren,[4] T. M. Liss,[13] J. B. Liu,[30] Y. C. Liu,[33] N. Lockyer,[26] O. Long,[26] M. Loreti,[25] D. Lucchesi,[27] P. Lukens,[7] S. Lusin,[40] J. Lys,[18] K. Maeshima,[7] P. Maksimovic,[11] M. Mangano,[27] M. Mariotti,[25] J. P. Marriner,[7] G. Martignon,[25] A. Martin,[41] J. A. J. Matthews,[22] P. Mazzanti,[2] K. McFarland,[30] P. McIntyre,[34] P. Melese,[31] M. Menguzzato,[25] A. Menzione,[27] E. Meschi,[27] S. Metzler,[26] C. Miao,[20] T. Miao,[7] G. Michail,[11] R. Miller,[21] H. Minato,[37] S. Miscetti,[9] M. Mishina,[17] S. Miyashita,[37] N. Moggi,[27] E. Moore,[22] Y. Morita,[17] A. Mukherjee,[7] T. Muller,[16] A. Munar,[27] P. Murat,[27] S. Murgia,[21] M. Musy,[36] H. Nakada,[37] T. Nakaya,[5] I. Nakano,[12] C. Nelson,[7] D. Neuberger,[16] C. Newman-Holmes,[7] C.-Y. P. Ngan,[19] L. Nodulman,[1] A. Nomerotski,[8] S. H. Oh,[6] T. Ohmoto,[12] T. Ohsugi,[12] R. Oishi,[37] M. Okabe,[37] T. Okusawa,[24] J. Olsen,[40] C. Pagliarone,[27] R. Paoletti,[27] V. Papadimitriou,[35] S. P. Pappas,[41] N. Parashar,[27] A. Parri,[9] J. Patrick,[7] G. Pauletta,[36] M. Paulini,[18] A. Perazzo,[27] L. Pescara,[25] M. D. Peters,[18] T. J. Phillips,[6] G. Piacentino,[27] M. Pillai,[30] K. T. Pitts,[7] R. Plunkett,[7] A. Pompos,[29] L. Pondrom,[40] J. Proudfoot,[1] F. Ptohos,[11] G. Punzi,[27] K. Ragan,[14] D. Reher,[18] M. Reischl,[16] A. Ribon,[25] F. Rimondi,[2] L. Ristori,[27] W. J. Robertson,[6] A. Robinson,[14] T. Rodrigo,[27] S. Rolli,[38] L. Rosenson,[19] R. Roser,[13] T. Saab,[14] W. K. Sakumoto,[30] D. Saltzberg,[4] A. Sansoni,[9] L. Santi,[36] H. Sato,[37] P. Schlabach,[7] E. E. Schmidt,[7] M. P. Schmidt,[41] A. Scott,[4] A. Scribano,[27] S. Segler,[7] S. Seidel,[22] Y. Seiya,[37] F. Semeria,[2] T. Shah,[19] M. D. Shapiro,[18] N. M. Shaw,[29] P. F. Shepard,[28] T. Shibayama,[37] M. Shimojima,[37] M. Shochet,[5] J. Siegrist,[18] A. Sill,[35] P. Sinervo,[14] P. Singh,[13] K. Sliwa,[38] C. Smith,[15] F. D. Snider,[15] J. Spalding,[7] T. Speer,[10] P. Sphicas,[19] F. Spinella,[27] M. Spiropulu,[11] L. Spiegel,[7] L. Stanco,[25] J. Steele,[40] A. Stefanini,[27] R. Ströhmer,[7a] J. Strologas,[13] F. Strumia, [10] D. Stuart,[7] K. Sumorok,[19] J. Suzuki,[37] T. Suzuki,[37] T. Takahashi,[24] T. Takano,[24] R. Takashima,[12] K. Takikawa,[37] M. Tanaka,[37] B. Tannenbaum,[4] F. Tartarelli,[27] W. Taylor,[14] M. Tecchio,[20] P. K. Teng,[33] Y. Teramoto,[24] K. Terashi,[37] S. Tether,[19] D. Theriot,[7] T. L. Thomas,[22] R. Thurman-Keup,[1] M. Timko,[38] P. Tipton,[30] A. Titov,[31] S. Tkaczyk,[7] D. Toback,[5] K. Tollefson,[30] A. Tollestrup,[7] H. Toyoda,[24] W. Trischuk,[14] J. F. de Troconiz,[11] S. Truitt,[20] J. Tseng,[19] N. Turini,[27] T. Uchida,[37] F. Ukegawa,[26] J. Valls,[32] S. C. van den Brink,[15] S. Vejcik, III,[20] G. Velev,[27] I. Volobouev,[18] R. Vidal,[7] R. Vilar,[7a] D. Vucinic,[19] R. G. Wagner,[1] R. L. Wagner,[7] J. Wahl,[5] N. B. Wallace,[27] A. M. Walsh,[32] C. Wang,[6] C. H. Wang,[33] M. J. Wang,[33] A. Warburton,[14] T. Watanabe,[37] T. Watts,[32] R. Webb,[34] C. Wei,[6] H. Wenzel,[16] W. C. Wester, III,[7] A. B. Wicklund,[1] E. Wicklund,[7] R. Wilkinson,[26] H. H. Williams,[26] P. Wilson,[7] B. L. Winer,[23] D. Winn,[20] D. Wolinski,[20] J. Wolinski,[21] S. Worm,[22] X. Wu,[10] J. Wyss,[27] A. Yagil,[7] W. Yao,[18]

K. Yasuoka,[37] G. P. Yeh,[7] P. Yeh,[33] J. Yoh,[7] C. Yosef,[21] T. Yoshida,[24] I. Yu,[7] A. Zanetti,[36] F. Zetti,[27] and S. Zucchelli[2]

(CDF Collaboration)

[1] *Argonne National Laboratory, Argonne, Illinois 60439*
[2] *Istituto Nazionale di Fisica Nucleare, University of Bologna, I-40127 Bologna, Italy*
[3] *Brandeis University, Waltham, Massachusetts 02254*
[4] *University of California at Los Angeles, Los Angeles, California 90024*
[5] *University of Chicago, Chicago, Illinois 60637*
[6] *Duke University, Durham, North Carolina 27708*
[7] *Fermi National Accelerator Laboratory, Batavia, Illinois 60510*
[8] *University of Florida, Gainesville, Florida 32611*
[9] *Laboratori Nazionali di Frascati, Istituto Nazionale di Fisica Nucleare, I-00044 Frascati, Italy*
[10] *University of Geneva, CH-1211 Geneva 4, Switzerland*
[11] *Harvard University, Cambridge, Massachusetts 02138*
[12] *Hiroshima University, Higashi-Hiroshima 724, Japan*
[13] *University of Illinois, Urbana, Illinois 61801*
[14] *Institute of Particle Physics, McGill University, Montreal H3A 2T8, and University of Toronto, Toronto M5S 1A7, Canada*
[15] *The Johns Hopkins University, Baltimore, Maryland 21218*
[16] *Institut für Experimentelle Kernphysik, Universität Karlsruhe, 76128 Karlsruhe, Germany*
[17] *National Laboratory for High Energy Physics (KEK), Tsukuba, Ibaraki 305, Japan*
[18] *Ernest Orlando Lawrence Berkeley National Laboratory, Berkeley, California 94720*
[19] *Massachusetts Institute of Technology, Cambridge, Massachusetts 02139*
[20] *University of Michigan, Ann Arbor, Michigan 48109*
[21] *Michigan State University, East Lansing, Michigan 48824*
[22] *University of New Mexico, Albuquerque, New Mexico 87131*
[23] *The Ohio State University, Columbus, Ohio 43210*
[24] *Osaka City University, Osaka 588, Japan*
[25] *Universita di Padova, Istituto Nazionale di Fisica Nucleare, Sezione di Padova, I-35131 Padova, Italy*
[26] *University of Pennsylvania, Philadelphia, Pennsylvania 19104*
[27] *Istituto Nazionale di Fisica Nucleare, University and Scuola Normale Superiore of Pisa, I-56100 Pisa, Italy*
[28] *University of Pittsburgh, Pittsburgh, Pennsylvania 15260*
[29] *Purdue University, West Lafayette, Indiana 47907*
[30] *University of Rochester, Rochester, New York 14627*
[31] *Rockefeller University, New York, New York 10021*
[32] *Rutgers University, Piscataway, New Jersey 08855*
[33] *Academia Sinica, Taipei, Taiwan 11530, Republic of China*
[34] *Texas A&M University, College Station, Texas 77843*
[35] *Texas Tech University, Lubbock, Texas 79409*
[36] *Istituto Nazionale di Fisica Nucleare, University of Trieste/ Udine, Italy*
[37] *University of Tsukuba, Tsukuba, Ibaraki 305, Japan*
[38] *Tufts University, Medford, Massachusetts 02155*
[39] *Waseda University, Tokyo 169, Japan*
[40] *University of Wisconsin, Madison, Wisconsin 53706*
[41] *Yale University, New Haven, Connecticut 06520*

Abstract

We report the first direct measurement of $b\bar{b}$ rapidity correlations in $p\bar{p}$ collisions at $\sqrt{s} = 1.8\,\mathrm{TeV}$. We select events with a high transverse momentum muon accompanied by a jet, and a second jet associated with a decay vertex displaced from the $p\bar{p}$ interaction vertex. Two independent samples are obtained corresponding to events with a forward ($2.0 < |\eta| < 2.6$) or central ($|\eta| < 0.6$) muon. We measure the ratio of forward to central $b\bar{b}$ production to be $0.361 \pm 0.033\,(\mathrm{stat})\,^{+0.015}_{-0.031}\,(\mathrm{syst})$, in good agreement with the next-to-leading order QCD result, $0.338^{+0.014}_{-0.097}$.

I. INTRODUCTION

The study of $b\bar{b}$ production in high energy $p\bar{p}$ collisions has proven to be a valuable tool for the quantitative testing of perturbative QCD. The b-quark mass is considered large enough ($m_b >> \Lambda_{\rm QCD}$) that the production cross section can be expressed as a series expansion in the strong coupling α_s, while the large semileptonic branching fraction and long lifetime of b hadrons provide convenient experimental signatures that serve to separate $b\bar{b}$ production from the large QCD backgrounds at a hadron collider. In this paper we present the first direct measurement of $b\bar{b}$ rapidity correlations in $p\bar{p}$ collisions at $\sqrt{s} = 1.8$ TeV. Specifically, we measure the ratio $R \equiv \sigma(2.0 < |y_{b_1}| < 2.6)/\sigma(|y_{b_1}| < 0.6)$, given that the second b quark is observed in the central rapidity range $|y_{b_2}| < 1.5$, and both quarks have transverse momentum $p_T > 25\,{\rm GeV}/c$ and are separated by an azimuthal opening angle $\Delta\phi$ exceeding 60°. By measuring the ratio of cross sections, we are able to significantly reduce the experimental uncertainty while retaining the relevant information on the shape of the rapidity distribution.

At leading order in perturbative QCD, $b\bar{b}$ pairs are produced through $q\bar{q}$ annihilation and gluon fusion (Fig. 1). The annihilation process proceeds exclusively through the s-channel and leads to a rapidity correlation $d\sigma/dt \sim (\cosh\Delta y)^{-2}$ at large $\Delta y = y_b - y_{\bar{b}}$ [1]. The gluon fusion process includes t-channel exchange diagrams that enhance the contribution from final states where the b and $\bar{b}$ are produced at small angles (in the center-of-mass) with respect to the beam and leads to a less-pronounced rapidity correlation, $d\sigma/dt \sim (\cosh\Delta y)^{-1}$. For either process, the partonic cross section is suppressed as the rapidity difference increases and it is expected that a $b\bar{b}$ pair will be found closely separated in rapidity.

In Fig. 2, we show representative Feynman diagrams for the three general next-to-leading order (NLO) $b\bar{b}$ production processes: (a) direct, (b) flavor excitation, and (c) gluon splitting. The first two processes lead to a broadening of the Δy distribution while the gluon splitting process leads to an enhancement for $\Delta y \approx 0$. For this analysis, we require a minimum azimuthal opening angle between the b and $\bar{b}$ decay products, which suppresses the contribution from gluon splitting, and the shape of the NLO Δy distribution is expected to be similar to the leading-order dependence described above. This is in direct contrast to measurements of the differential cross section $d\sigma/d(\Delta\phi)$, which are directly sensitive to the relative contributions of the different NLO production processes due to the trivial leading order $\Delta\phi$ dependence.

The strong rapidity correlation predicted by QCD has practical consequences in the design of forward spectrometer experiments seeking to efficiently collect $b\bar{b}$ pairs for use in *CP*-violation studies, since it implies that if a b quark is detected in the forward region there is a high probability that the $\bar{b}$ is also forward. Accurate knowledge of the $b\bar{b}$ acceptance is critical to the optimal design of such detectors. Since the acceptance calculation is based on theory, it is important to experimentally verify that the rapidity correlation predicted by QCD is correct.

The observed $b\bar{b}$ rapidity correlation also depends on the parton distribution functions (PDFs) inside the proton. In particular, production of high-momentum b hadrons in the forward region is sensitive to the PDFs at large momentum fraction x. Since the gluon fusion process dominates the $b\bar{b}$ production cross section, the shape of the b-quark rapidity distribution at large y is sensitive to the shape of the gluon distribution $G(x, Q^2)$ at large x.

The observation of an excess of high transverse energy jets reported by the Collider Detector at Fermilab (CDF) collaboration [2] has led to increased interest in the high-x gluon content of the proton [3]. It has recently been demonstrated that $G(x, Q^2)$ in the region $x < 0.15$ is indirectly constrained to within 10% by Drell-Yan and deep-inelastic scattering data, but is essentially unconstrained at higher values [4]. Historically, direct photon production, through the Compton scattering process $gq \to \gamma q$, has provided the only direct constraint on $G(x, Q^2)$ for $x > 0.15$. However, the full sensitivity of this process has yet to be realized due to the uncertainty in the correct modeling of initial-state transverse momentum (k_T) [5,6]. An accurate measurement of forward b production could provide an important additional constraint on the gluon distribution at high x.

The majority of bottom-production measurements at $p\bar{p}$ colliders have been restricted to the central region; $|y_b| < 1.5$ for the UA1 measurements at CERN [7], and $|y_b| < 1.0$ for the CDF [8] and DØ [9] measurements at the Tevatron. The absence of precision track reconstruction capabilities in the forward region severely limits the techniques available for separating $b\bar{b}$ events from the large background of multijet events at a hadron collider. In addition, particles from the proton remnant and uncorrelated beam-gas collisions populate the region near the beam line, further complicating identification of the b-hadron decay products at the highest accessible rapidity.

The DØ collaboration was the first to report a forward b production measurement at a hadron collider [10]. They identified muons in the rapidity range $2.4 < |y| < 3.2$ and determined the fraction of muons from b decay by first subtracting the expected shape and normalization of the p_T spectrum for muons from the decay of light mesons (π, K). The remaining events were attributed to bottom and charm production and the relative amount of each process was determined from Monte Carlo predictions. The result agrees in the shape of the p_T spectrum, but with a normalization in excess of the central value predicted by NLO QCD [11] by a factor of four. This discrepancy is beyond current estimates of the theoretical uncertainty from perturbative effects, which amount to an overall factor of two. In contrast, the theoretical uncertainty does account for the smaller normalization excess observed in measurements of central $b\bar{b}$ production [12].

Recent studies by two separate groups show that an increase in the forward cross section can be obtained by modifying the heavy-quark fragmentation function [13], or by employing the variable-flavor-number perturbative calculation [14] rather than the fixed-flavor scheme used in Ref. [11]. However, the increase in both cases is insufficient to account for the $D\emptyset$ result. An independent measurement in the forward region provides an additional constraint on possible explanations of the discrepancy between data and theory observed by $D\emptyset$.

For the analysis presented in this paper, we measure the ratio of the double differential cross section $d^2\sigma/dy_1dy_2$ for two orthogonal topologies: forward-central, where one quark is produced in the rapidity range $2.0 < |y_1| < 2.6$ and the second satisfies $|y_2| < 1.5$, and central-central, where $|y_1| < 0.6$ and $|y_2| < 1.5$. By simultaneously measuring the ratio of forward and central $b\bar{b}$ cross sections using similar data samples with identical kinematic requirements, we are able to eliminate or significantly reduce many of the experimental systematic uncertainties. In addition, identification of the second b quark in the central detector allows the use of microvertexing techniques to suppress background from processes that do not produce heavy quarks.

The data used for this analysis correspond to $77\,\mathrm{pb}^{-1}$ of $p\bar{p}$ collisions collected by CDF between January 1994 and July 1995 (Run 1B). We use forward and central high-p_T muon triggers to accumulate two independent samples enriched in forward and central b decays, respectively. The fraction of muons from b decay is determined by identifying a jet associated with the trigger muon and fitting the distribution of muon transverse momentum relative to the jet axis, p_T^{rel}. The long lifetime of b hadrons is exploited by identifying the second b quark as a central jet associated with a decay vertex (secondary vertex) displaced from the $p\bar{p}$ interaction vertex (primary vertex). An updated version of the b-tagging algorithm developed for the CDF top-quark analyses is used to "tag" jets likely to contain a heavy quark. Real b jets are separated from charm, light quark, and gluon jets by fitting the distribution of transverse decay length ct of the secondary vertex.

The remainder of this paper is organized as follows. Section II describes the detector and trigger systems used to identify muons, jets, and displaced vertices. Section III describes the selection criteria used to isolate a sample of events consistent with $b\bar{b}$ production, and Section IV describes the efficiency and acceptance for detecting $b\bar{b}$ events passing the analysis cuts. In Section V, we describe the fitting procedure used to determine the $b\bar{b}$ purity in our data, and several consistency checks on the fit results. The cross section ratio is presented and analyzed in Section VI, and we summarize the analysis in Section VII.

II. DETECTOR

The CDF has been described in detail elsewhere [15]. We use a cylindrical coordinate system (r, ϕ, z) with the z axis aligned along the proton beam direction. Polar angle θ and azimuthal angle ϕ are measured from the z and x axes, respectively, and transverse quantities correspond to projections in the r-ϕ plane. In this section we describe the tracking, muon, calorimeter, and trigger subsystems used to identify muons, jets, and displaced vertices from b decay.

A. Tracking System

Charged particle trajectories are reconstructed using the CDF central tracking system, which consists of three complementary detectors immersed in a 1.4 T solenoidal magnetic field aligned along $\hat{z}$. Closest to the beam, a silicon microvertex detector (SVX) [16,17] provides precision spatial resolution in the transverse plane. The device consists of four concentric layers of silicon strip detectors grouped into two modules extending 25.5 cm in each direction along the beam line. The inner and outer detector layers are at radii of 2.9 and 7.9 cm, respectively. The impact parameter resolution is measured to be $\sim (13 + 40/p_T)\ \mu$m for isolated tracks, where p_T is the transverse momentum in GeV/c.

Just outside the SVX, a set of vertex time projection chambers (VTX) measure charge particle trajectories in the r-z plane to a radius of 22 cm and over the pseudorapidity range $|\eta| < 3.25$. During Run 1B, $p\bar{p}$ collisions were distributed along z according to a Gaussian distribution with $\bar{z} = 0$, and $\sigma_z \approx 30$ cm. Information from the VTX is used to measure the z position of the $p\bar{p}$ interaction vertex with an accuracy of ~ 1 mm.

The outermost tracking detector, the central tracking chamber (CTC) [18], provides full three-dimensional track reconstruction to a radius of 132 cm. The CTC is a cylindrical drift chamber consisting of 84 layers of sense wires grouped into alternating axial and $\pm 3°$ stereo superlayers. Fast timing information from the CTC was used to identify events containing a high-p_T track early in the trigger process, while tracks reconstructed offline were used for central-muon momentum measurements, and as seeds for SVX pattern recognition. The momentum resolution of the CDF tracking system is $\delta p_T/p_T = \sqrt{(0.002p_T)^2 + (0.0066)^2}$ for CTC tracks, where p_T is in GeV/c. The resolution improves to $\sqrt{(0.0009p_T)^2 + (0.0066)^2}$ for tracks using both CTC and SVX information.

B. Muon Systems

The CDF muon systems used in this analysis are the central muon (CMU) [19], central muon upgrade (CMP),

and forward muon (FMU) [20] detectors. Located just outside the 5 absorption lengths (at normal incidence) of material comprising the central hadron calorimeter, the CMU consists of four layers of drift chambers with sense wires aligned parallel to the beam direction. The CMP is located behind an additional 60 cm of steel absorber and consists of four more layers of axially-aligned drift chambers. Requiring CMP hits substantially reduces the background from hadrons escaping the central calorimeter. CMU and CMP segments are defined as sets of two or more hits in each detector, and a central-muon candidate is identified by matching a CTC track with both a CMU and CMP segment in ϕ and z. Charge division in the CMU is used to measure the z position of the muon segment. The combined CMU-CMP system covers 53% of the solid angle for $|\eta| < 0.6$. Identified central-muon candidates are referred to as CMUP muons.

The FMU is a forward/backward magnetic spectrometer consisting of three planes of drift chambers sandwiching two 1 m-thick iron toroids. The detector planes (front, middle, rear) are located at $|z| \approx 10, 11.5, 13$ m and are divided into 24 chambers, each covering 15° in ϕ and staggered in z to allow for overlap at the edges. The chambers consist of two planes of half-cell staggered drift cells separated by a copper cathode plane, with each cell containing a sense wire strung along a chord in azimuth. Cell size increases with increasing r and z to provide a projective tower geometry for triggering. The cathode plane is divided into 15 "pads", each covering 5° in ϕ and 3° in θ, which provide the ϕ position of reconstructed FMU tracks. In addition, two planes of scintillator with 5° azimuthal segmentation cover the front and rear detector planes. A forward muon candidate consists of 6 drift chamber hits projecting back to the interaction point, 3 cathode pad hits aligned in η and ϕ, and 2 scintillator hits matching the pad hits in ϕ.

The FMU toroids are instrumented with four 28-turn copper coils each carrying a current of 600 A, generating an azimuthal magnetic field varying from 1.96 T at the inner radius (50 cm) to 1.58 T at the outer radius (380 cm). Tracks are reconstructed from drift chamber hits using an iterative fitting procedure which takes into account multiple Coulomb scattering and energy loss in the toroids. The track momentum is determined from the fitted curvature in the magnetic field region, and the resolution is $\delta p_T/p_T \approx 15\%$. The FMU system covers the full solid angle for the pseudorapidity range $1.9 < |\eta| < 3.7$.

C. Calorimeter Systems and Jet Identification

The CDF calorimeter system [21] comprises central ($|\eta| < 1.1$), plug ($1.1 < |\eta| < 2.4$), and forward ($2.4 < |\eta| < 4.2$) regions divided into electromagnetic (lead absorber) and hadronic (iron absorber) compartments. Each calorimeter is segmented in η and ϕ to provide a projective tower geometry. The central calorimeters use scintillator as the active medium and have a tower size of $\Delta\eta \times \Delta\phi = 0.1 \times 15°$. The plug and forward calorimeters use gas as the active medium and have a tower size of $\Delta\eta \times \Delta\phi = 0.1 \times 5°$.

Jets are identified as clusters of energy deposition in the calorimeters using a fixed-cone clustering algorithm [22]. We use a cone size of $R = \sqrt{\Delta\eta^2 + \Delta\phi^2} = 0.7$ for this analysis. The total jet energy, defined as the scalar sum of measured energies in the towers assigned to the jet, is corrected for detector effects (including η-dependent corrections) and underlying event energy using the standard CDF corrections [23]. The jet momentum vector is calculated assuming the energy in each tower was deposited by a single massless particle originating from the primary vertex. The direction of this vector defines the jet axis that we use to calculate $p_T^{\rm rel}$ for the muons in this analysis. We distinguish between jet pseudorapidity η and detector pseudorapidity η_D, where the latter uses $z = 0$. The approximate jet energy resolution is $(0.1p_T + 1.0)$ GeV, where p_T is in GeV/c [24].

D. Trigger System

The CDF trigger system [25] is divided into first and second level hardware triggers and a third level software trigger based on a version of the offline reconstruction package optimized for execution speed. This analysis uses data acquired with the inclusive central muon and forward muon+jet triggers.

1. Central Muon Trigger

The level 1 high-p_T central-muon trigger required matching CMU and CMP segments corresponding to a nominal p_T threshold of 6 GeV/c. A coarse p_T measurement is achieved by exploiting the fact that low momentum tracks emerge from the magnetic field at an angle with respect to the radial direction, producing different arrival times on the radially-aligned wires of the CMU detector. The level 2 trigger required a match within 5° in ϕ between the CMU segment and a two-dimensional (r-ϕ) CTC track found by the central fast tracker (CFT) [26]. The CFT is a dedicated hardware track processor programmed to identify predetermined hit patterns corresponding to p_T thresholds from 2.2 to 27 GeV/c. The matched CFT track was required to have $p_T > 7.5$ GeV/c and this trigger had its rate reduced (prescaled) by accepting a fraction of the events based on the instantaneous luminosity. The level 3 trigger performed full three-dimensional tracking and required CMU and CMP segments matched to a CTC track with $p_T > 6$ GeV/c. Approximately 7 million events were collected with the central muon trigger.

2. Forward Muon+Jet Trigger

The FMU level 1 trigger employed pattern recognition units to search for sets of 6 drift chamber hits, 3 cathode pad hits, and 2 scintillator hits consistent with the expected signature of a high-p_T muon originating from the interaction point. Track candidates were identified as sets of drift chamber hits satisfying a tight trigger road in η, while sets of pad hits aligned within 5° in ϕ and 3° in θ were matched to front-rear scintillator pairs within 5° in ϕ. The trigger required the presence of a track candidate and pad-scintillator match in the same ϕ octant, and was approximately 50% efficient at 7.5 GeV/c. The maximum rate for this trigger was limited to 0.6 Hz during Run 1B.

No additional requirements were applied at level 2. At level 3, the FMU track reconstruction code was executed, and the trigger required at least one track with $p_T > 4\,\mathrm{GeV}/c$. Although the FMU was instrumented to $|\eta| = 3.7$, large backgrounds near the Tevatron beam pipe restricted the active trigger coverage to $1.9 < |\eta| < 2.7$. Further background suppression of sources not associated with the $p\bar{p}$ collision was accomplished by requiring the total number of sense wire hits in the active region of the trigger octant to be less than 31, corresponding to a maximum occupancy of 13%. Finally, real muon backgrounds from the decay of vector bosons and light mesons were suppressed relative to heavy-quark decays by requiring at least one jet in the event with uncorrected $E_T > 20\,\mathrm{GeV}$. Approximately 150,000 events were collected with the forward muon+jet trigger.

III. EVENT SELECTION

The selection criteria applied in this analysis are designed to detect both the b and $\bar{b}$ by identifying the semileptonic decay of one b hadron to a muon and jet, and the inclusive decay of the second b hadron using a secondary-vertex tagging algorithm. The muon and the jet containing it are collectively referred to as the μ tag, while the jet tagged by the secondary vertexing algorithm is referred to as the SVX tag. Events are classified as forward or central depending on whether the muon is FMU or CMUP, respectively. This section describes the cuts used to define the forward and central samples.

Beginning with the two muon-triggered data samples, a three-dimensional primary vertex location was determined event-by-event by combining the VTX z position, the average Tevatron beam line position, and SVX tracks, where tracks with large impact parameters with respect to the fitted vertex were removed by an iterative procedure. The resulting vertex was required to have $|z| < 30\,\mathrm{cm}$ to keep events in the region of good SVX acceptance. Jets were then reclustered with respect to this vertex and all FMU tracks were refit using the new vertex as a constraint.

A. μ Tag Requirements

Forward and central muon candidates are required to pass their respective trigger criteria. Poorly measured forward muons are rejected by requiring that the track-fit confidence level exceed 1%. Central muons must satisfy tight segment-track matching requirements. The position of the CTC track extrapolated to the muon chambers must match within 3σ in ϕ and $\sqrt{12}\sigma$ in z, where σ is the rms spread due to multiple Coulomb scattering taking into account energy loss in the calorimeters. The track is also required to point to the primary vertex within 5 cm in z. We require a minimum muon p_T of $6\,\mathrm{GeV}/c$ for both samples. Forward muons are restricted to the pseudorapidity range $2.0 < |\eta| < 2.6$ to match the extent of the CMU coverage ($|\eta| < 0.6$). In each event, the highest-p_T muon passing all of the above cuts is used. The μ jet is then identified as the jet with the minimum separation in η-ϕ space from the muon. This separation is required to be < 0.7 and the μ-jet candidate must have corrected $E_T > 15\,\mathrm{GeV}$. Forward and central μ jets are restricted to the regions $1.9 < |\eta_D| < 2.7$ and $|\eta_D| < 0.7$, respectively.

B. SVX Tag Requirements

The SVX tag is identified as a central jet ($|\eta_D| < 1.5$) with corrected $E_T > 26\,\mathrm{GeV}$ and tagged by the CDF secondary-vertexing algorithm (SECVTX) [27]. The algorithm begins by assigning SVX tracks to the nearest jet within a cone of 0.7, where track pairs consistent with K_S or Λ decays are removed from the list. The strategy is to make a first attempt at finding a vertex using loose track cuts but requiring ≥ 3 tracks in the tag. The track quality cuts include $p_T > 0.5\,\mathrm{GeV}/c$ and impact parameter significance $d_0/\sigma_{d_0} > 2.5$, where d_0 is the distance between the track and primary vertex in the transverse plane at closest approach to the vertex. In addition, the highest p_T track must have $p_T > 2.0\,\mathrm{GeV}/c$. If this attempt fails, tighter track cuts ($p_T > 1.0\,\mathrm{GeV}/c$, $d_0/\sigma_{d_0} > 3.0$) are applied and a vertex with ≥ 2 tracks is required. If a vertex is found, the signed transverse decay length L_{xy} is defined as the projection of the two-dimensional vector from the primary to the secondary vertex onto the jet axis in the transverse plane. We require $|L_{xy}|/\sigma \geq 2.0$, where σ is the total error on L_{xy}, including the contribution from the primary-vertex fit. The efficiency for tagging b jets is determined from Monte Carlo to be 45%, and is approximately equal in the forward and central samples. There are 391 forward and 7737 central events containing both a μ tag and SVX tag.

C. Opening Angle Requirement

There is one final cut applied to both samples. Once the SVX tag is identified, we require $\Delta\phi(\text{tags}) > 60°$, where $\Delta\phi$ is the azimuthal opening angle between the SVX-tag jet axis and the vector sum of the muon and μ-jet momenta. The motivation for this cut is illustrated in Fig. 3, where we show the observed $\Delta\phi(\text{tags})$ distributions in the forward and central data samples, compared with the corresponding $b\bar{b}$ $\Delta\phi$ distributions from the NLO QCD calculation of Mangano, Nason, and Ridolfi (MNR) [11]. The gluon splitting process produces $b\bar{b}$ pairs that are closely separated in η-ϕ space, leading to an enhancement in the cross section for $\Delta\phi \approx 0$. By definition, the forward-central topology requires a minimum $b\bar{b}$ opening angle and no such enhancement is observed, either in the QCD prediction or in the data. For the central-central topology, the b and $\bar{b}$ can occupy overlapping regions in η-ϕ space, and QCD predicts a significant gluon splitting contribution. However, the event yield in the central sample is observed to decrease for $\Delta\phi < 60°$ due to the requirement that the b and $\bar{b}$ decay products are reconstructed as separate jets. The presence of the gluon splitting process in only the central sample leads to a model dependence in the acceptance calculation that does not cancel in the cross section ratio. By requiring $\Delta\phi(\text{tags}) > 60°$, we explicitly remove the contribution from gluon splitting, which allows us to ignore this process in the acceptance calculation. Our measurement is therefore insensitive to gluon splitting production. There are 382 (7544) forward (central) events remaining after the $\Delta\phi$ cut.

IV. EFFICIENCY AND ACCEPTANCE

In this section we describe the efficiency and acceptance for detecting forward and central $b\bar{b}$ events satisfying the triggers and offline cuts applied in this analysis.

A. Forward Muon Efficiency

The efficiency of the 0.6 Hz rate limit on the FMU level 1 trigger was calculated to be 39.6% and is included in the acceptance calculation. The remaining trigger requirements are decomposed into kinematic and detector efficiencies. The kinematic efficiency, included in the acceptance calculation, is defined as the probability that a muon of a given p_T will produce a set of 6 drift chamber hits satisfying the trigger pattern for a detector with 100% detector efficiency. The detector efficiency is defined as the product of drift chamber, cathode pad, scintillator, and trigger electronics efficiencies and is measured in a sample of $Z^0 \to \mu^+\mu^-$ decays, where the trigger muon is CMUP and the second muon is FMU. Figure 4 shows the dimuon mass distribution for muon pairs with opposite charge. The fraction of same-charge events in the total sample is 3.5%, indicating a correspondingly small fake background in the opposite-charge sample. The combined efficiency for requiring 6 drift chamber hits, 3 pad hits, and 2 scintillator hits is $71.4 \pm 1.6\%$.

The level 3 occupancy cut required < 31 drift chamber hits in the trigger octant. The efficiency of this cut was measured in a sample of FMU level 1 triggers rejected by the 0.6 Hz rate limit, but subsequently accepted through an independent trigger path. Figure 5 shows the efficiency as a function of instantaneous luminosity. We perform a linear fit constraining $\epsilon(\mathcal{L} = 0) = 1.0$ and convolute the resulting functional form with the luminosity distribution observed in events passing the FMU level 1 trigger. The resulting efficiency is $88.5 \pm 0.4 \pm 0.5\%$, where the first uncertainty is statistical and the second is due to uncertainty on the fitted slope.

The efficiency of the level 3 jet requirement was measured in a sample of events passing the inclusive FMU trigger and containing a jet with corrected $E_T > 26\,\text{GeV}$ and $|\eta_D| < 1.5$. The inclusive trigger required a muon passing the same cuts as the FMU+jet trigger, but with a higher p_T threshold ($15\,\text{GeV}/c$). The efficiency, calculated as the fraction of events in the sample that pass the FMU+jet trigger, was found to be $98.6 \pm 0.3\%$.

The efficiency of the confidence-level cut on the FMU track fit was measured in the same CMUP-FMU Z^0 sample used to measure the level 1 detector efficiency. We find the efficiency for requiring a confidence level exceeding 1% to be $92.0 \pm 1.0\%$. This result is consistent with the efficiency determined from a detailed Monte Carlo simulation of the FMU detector as well as the efficiency measured directly in the forward muon+jet trigger sample.

B. Central Muon Efficiency

The level 1 CMU and CMP segment-finding efficiencies were measured in a sample of $Z^0 \to \mu^+\mu^-$ events by comparing the number of muon segments with 3 drift chamber hits to the number with 4 hits, from which the single hit efficiency was derived. The combined efficiency for requiring 2 or more hits in both the CMU and CMP detectors is $98.1 \pm 0.3\%$. The efficiency of offline matching requirements between the CTC track and muon segments was measured in a sample of $J/\psi \to \mu^+\mu^-$ events to be $98.5 \pm 0.2\%$. The segment-finding and track-matching efficiencies are combined into a CMUP identification efficiency of $96.6 \pm 0.4\%$.

The central muon trigger efficiencies were measured in independently triggered samples of J/ψ and Z^0 events. The level 3 plateau efficiency was measured to be $98.5 \pm 1.0\%$, while the level 1 and level 2 triggers are parameterized as a function of p_T and included in the trigger simulation as part of the acceptance calculation. The efficiency of the level 2 prescale was calculated to be 55.9%

and is also included in the central muon trigger simulation.

The track-finding efficiency in the CTC was studied by embedding Monte Carlo tracks into real J/ψ events [28,29]. For $p_T > 1\,\mathrm{GeV}/c$ the tracking efficiency is constant and measured to be $96.2 \pm 0.9\%$, where the uncertainty is statistical only.

C. Acceptance

The acceptance calculation includes the muon geometric and kinematic cuts, trigger efficiency, jet identification, and b-tagging requirements in one Monte Carlo program. The acceptance is defined as the number of events satisfying all cuts divided by the number of generated events satisfying the cross section cuts (defined below).

The Monte Carlo program uses ISAJET [30] version 7.06 to generate $b\bar{b}$ events with MRSA$'$ [31] PDFs, Peterson fragmentation with $\epsilon = 0.006$ [32,33], and a b-quark mass of $4.75\,\mathrm{GeV}/c^2$. The event z-vertex position is chosen randomly from a Gaussian distribution with $\bar{z} = 0$ and $\sigma_z = 29\,\mathrm{cm}$. Since the efficiency of the z-vertex cut cancels in the cross section ratio, events are only generated in the range $|z| < 30\,\mathrm{cm}$. ISAJET treats the direct, flavor excitation, and gluon splitting production processes as incoherent and any difference in acceptance will lead to a dependence on the relative cross sections. Fortunately, we find that the acceptance for the direct and flavor excitation processes are equal within Monte Carlo statistics and the gluon-splitting process is negligible after the $\Delta\phi > 60^\circ$ requirement. The acceptance calculation is therefore defined with respect to direct production only. We have confirmed that the ISAJET p_T and η distributions for the b and $\bar{b}$ agree with the full NLO calculation.

The CLEO Monte Carlo program, QQ [34], is used to model the b-hadron decays, where the full decay table is used to include the effects of sequential decays ($b \to c \to \mu$). The muon branching fraction, defined as the fraction of all $b\bar{b}$ events that produce a muon from heavy-quark decay, cancels in the cross section ratio. The branching fraction is therefore removed from the acceptance calculation by redecaying events until at least one b quark produces a muon in its decay chain.

Generated events are simulated using the full CDF simulation package. The central muon trigger is simulated by applying the measured level 1 and level 2 trigger efficiency parameterizations, including the effect of the prescale on the $7.5\,\mathrm{GeV}/c$ level 2 trigger. The forward muon level 1 trigger is simulated by requiring that the drift chamber hits used in reconstructing the track satisfy the trigger pattern. The FMU detector simulation includes extra hits from delta rays and muon bremsstrahlung distributed according to the results of a detailed model of multiple scattering and energy loss in the calorimeters and toroids. Events satisfying the trigger are treated like real data, requiring both a μ tag and SVX tag passing the offline cuts.

The acceptance is calculated separately for the forward and central topologies using two independently generated Monte Carlo samples. Forward events were generated with both quarks having $p_T > 15\,\mathrm{GeV}/c$, one quark in the rapidity range $1.65 < |y| < 3.0$, and the second quark with $|y| < 1.65$. Central events were generated with the same p_T threshold and a rapidity requirement of $|y| < 1.65$ for both quarks. These cuts were designed to minimize any bias by extending into the regions of zero acceptance. The criteria used to define the forward and central cross sections are determined in the following way. First, the rapidity range of the trigger b is set equal to the muon pseudorapidity range in each sample, while the rapidity range of the second b is set equal to the pseudorapidity range of the SVX tag. The minimum p_T is then defined such that 90% of events satisfying all cuts originate from $b\bar{b}$ events where both quarks have $p_T > p_T^{\mathrm{min}}$. We find $p_T^{\mathrm{min}} = 25\,\mathrm{GeV}/c$ for both samples. With this definition, the acceptance for the forward sample, including the efficiency (39.6%) of the level 1 rate limit, is $(7.73 \pm 0.09) \times 10^{-3}$. The corresponding acceptance for the central sample is $(2.54 \pm 0.06) \times 10^{-2}$. The uncertainty in both cases is statistical only. The smaller acceptance in the forward sample is due almost entirely to the lower kinematic acceptance of the toroids relative to the central detectors and the steeper $d\sigma/dp_T$ production spectrum in forward $b\bar{b}$ events.

The total efficiency for detecting a forward or central topology combines the efficiency measurements and acceptance calculation described above. Tables I and II summarize the results for the forward and central samples, respectively. The relative efficiency (central/forward) is 5.24 ± 0.21.

V. FITTING PROCEDURE AND RESULTS

There are several physics processes besides $b\bar{b}$ production that contribute to the data samples described in Sec. III. These include $c\bar{c}$ production, heavy-quark production in association with a high-p_T gluon or light-quark jet that fakes a μ tag or SVX tag, generic dijet events producing two fake tags, and $Z^0 \to b\bar{b}$ decay. Four-heavy-quark production ($b\bar{b}b\bar{b}$, $b\bar{b}c\bar{c}$, $c\bar{c}c\bar{c}$) has been calculated to leading order [35] and is estimated to be negligible. We determine the fraction of events in each sample consisting of two real b tags by simultaneously fitting the p_T of the muon relative to the μ-jet direction, and the transverse proper decay length of the SVX tag. The number of $b\bar{b}$ events due to Z^0 decay is then estimated using the CDF measured cross section and a Monte Carlo acceptance calculation. The remainder of this section describes the templates used in the fit, the fit results and Z^0 subtraction, and several consistency checks.

A. Templates

1. Pseudo-ct

The transverse proper decay length of the secondary vertex is estimated with the following equation,

$$\text{pseudo-}ct = L_{xy}\frac{M}{p_T}, \tag{1}$$

where the mass M and p_T are calculated with the assumption that the tracks used in the tag are pions, and "pseudo" refers to the fact that we do not fully reconstruct the b hadron. In Fig. 6, we show the pseudo-ct distributions used as templates for bottom, charm, and fake SVX tags, where "fake" tags are defined as tagged jets which do not contain a heavy quark. The shape of the b quark distribution is obtained from the Monte Carlo samples used in the acceptance calculation. A similar Monte Carlo simulation is used to generate forward and central samples of $c\bar{c}$ events passing the same requirements as the $b\bar{b}$ samples. The shapes of the bottom and charm pseudo-ct distributions in the forward sample are similar to the corresponding distributions in the central sample.

The fake SVX-tag distribution is constructed in the following way. First, we note that fake tags from random track combinations are due to track reconstruction errors, leading to non-Gaussian tails in the SVX resolution function, and are symmetric with respect to $ct = 0$ [27]. Second, based on the bottom and charm Monte Carlo distributions in Fig. 6, the fraction of heavy-quark tags with $L_{xy} < 0$ is small ($\sim 1\%$). We therefore assume that the negative tags in a sample of inclusive jet events will be dominated by fake tags and derive the fake SVX-tag pseudo-ct template by symmetrizing the distribution of negative tags with respect to $ct = 0$. The jet sample was obtained from events collected with three inclusive jet triggers with thresholds of 20, 50, and 100 GeV/c. The resulting fake pseudo-ct template is displayed in the bottom plot of Fig. 6. Although this procedure ignores some sources of real secondary vertices from the decay of long-lived particles, the tagging algorithm explicitly removes the majority of K_S and Λ decays, and the CDF track reconstruction algorithm removes tracks with a large kink that would arise from π or K decays. Several checks on the pseudo-ct fit results are presented in Sec. V C.

2. $p_T^{\rm rel}$

Due to the large b-quark mass, muons from b decay are, on average, more energetic and have a larger opening angle relative to the remaining decay products than do muons from the decay of hadrons containing charm or lighter quarks. This information is contained in the variable $p_T^{\rm rel}$, defined as the muon p_T relative to the μ-jet axis,

$$p_T^{\rm rel} = p^{\mu}\sin\alpha, \tag{2}$$

where α is the angle between the muon and μ-jet momentum vectors and p^{μ} is the total muon momentum. When determining α, the muon minimum ionizing energy deposited in the calorimeter is not subtracted from the μ-jet momentum vector. Although more precise techniques for determining the b purity exist in the central region of the CDF, the absence of precision track information capable of identifying secondary vertices in the forward region leaves $p_T^{\rm rel}$ as the only variable capable of separating b decays from background. Using the same method in both samples acts as an indirect check on the forward fit result.

The default CDF calorimeter simulation does not accurately reproduce event-by-event fluctuations in the position of the μ-jet energy centroid relative to the muon direction. It was therefore necessary to develop a smearing procedure in order to obtain good agreement between data and Monte Carlo $p_T^{\rm rel}$ distributions. The procedure, a more detailed description of which is presented in Ref. [36], consists of smearing the η and ϕ position of the μ-jet axis according to a Gaussian distribution for some fraction of events. The width of the Gaussian and fraction of events to smear are then tuned to reproduce the observed $\Delta\phi$ and $\Delta\eta$ distributions between the μ-jet axis determined from calorimeter vs. tracking information. This choice of calibration variable is motivated by the good agreement between data and default Monte Carlo $p_T^{\rm rel}$ distributions when the μ-jet axis is obtained from CTC tracks. We apply the same smearing procedure to signal and background Monte Carlo samples in the forward and central regions.

In Fig. 7, we compare the $p_T^{\rm rel}$ distribution obtained from the central $b\bar{b}$ smeared Monte Carlo sample to the subsample of central data events where the μ jet is also tagged by SECVTX (double-tagged sample). The b purity in this sample is $> 90\%$ and the smeared Monte Carlo reproduces the shape of the $p_T^{\rm rel}$ distribution. The shape of the smeared $p_T^{\rm rel}$ distribution in the forward sample is very similar to the central sample (Fig. 8).

Figure 9 shows the $p_T^{\rm rel}$ template distributions for muons from charm and light-meson decays obtained with the same smearing procedure applied to the $b\bar{b}$ Monte Carlo events. Muons from π and K decay are modeled by generating gluon and light-quark events in ISAJET and decaying the produced mesons according to their muon branching fractions and lifetimes. Muons descended from mesons that decay before showering in the calorimeter are simulated and subjected to the same requirements placed on muons from heavy-quark decay. The μ tags from decay-in-flight muons are referred to as "fake". We find that the $p_T^{\rm rel}$ resolution is insufficient to separate fake muons from charm-decay muons. We therefore use the charm distribution to represent both components in the fit, and quote the difference obtained by using the fake template as a systematic uncertainty.

B. Fit Results

With the possibility of having bottom (b), charm (c), and fake (f) tags, there are 9 distinct combinations of SVX and μ tags. However, we do not consider four-heavy-quark production (which excludes the two components with one bottom and one charm tag) and $p_T^{\rm rel}$ does not distinguish charm and fake μ tags, so there are five distinct components in the fit. We label these five components f_{bb}, f_{cc}, f_{bf}, f_{fb}, and f_{fc}, where the first and second indices indicate the source of SVX and μ tags, respectively. The component f_{cc} includes the background combination involving a charm SVX tag and fake μ tag, and f_{fc} includes the background combination with two fake tags. We perform a simultaneous binned maximum likelihood fit using pseudo-ct and $p_T^{\rm rel}$ to determine the relative contribution from these five processes, where the $p_T^{\rm rel}$ fit is separated into events with positive and negative L_{xy}. With the assumption that the negative tags are predominantly fake, this procedure enables the individual determination of the two components with fake SVX tags (f_{fb} and f_{fc}). The only constraint in the fit is that all components must be positive. The fit results are listed in Table III. The χ^2 per degree of freedom is 1.1 and 1.4 for the forward and central fits, respectively. Combining the fitted signal fractions with the total number of events in each dataset, we determine that 311 ± 23 forward and 4655 ± 128 central events are due to $b\bar{b}$ production where both quarks are correctly identified.

We show the pseudo-ct and $p_T^{\rm rel}$ fit results for the forward sample in Fig. 10 and for the central sample in Fig. 11. For the $p_T^{\rm rel}$ fits, the main plot shows the distribution in events where the SVX tag has positive L_{xy}, while the inset shows the events with a negative L_{xy} tag. Overall, the fit results are very good. In particular, the fake SVX-tag template obtained from jet data reproduces the shape of the negative pseudo-ct distribution in both samples, and the smeared Monte Carlo $p_T^{\rm rel}$ templates provide a good fit on the μ-tag side.

The expected number of $b\bar{b}$ events due to Z^0 decay is estimated from the $Z^0 \to e^+e^-$ cross section measured by CDF [37], the luminosity ($77\,{\rm pb}^{-1}$), the relative branching fractions [38], and a calculation of the acceptance for detecting $b\bar{b}$ events from Z^0 decay using the same Monte Carlo simulation described in Sec. IV C. We determine that 4.1 ± 0.7 forward, and 203 ± 33 central $b\bar{b}$ events are due to Z^0 decay. These estimated event yields are subtracted from the fitted number of $b\bar{b}$ events in each sample, resulting in a final estimate of 307 ± 23 forward and 4452 ± 132 central $b\bar{b}$ events.

C. Consistency Checks

In constructing the fake SVX-tag pseudo-ct template, we assume that the fraction of negative tags in a sample of bottom and charm events is small ($\sim$ 1%). To check this assumption, in Fig. 12 we compare the $b\bar{b}$ Monte Carlo template to the distribution obtained from the double-tagged central data. The agreement is very good, giving confidence that the fraction of negative tags in a sample of heavy-quark decays is properly modeled by the Monte Carlo simulation.

The second assumption we make when constructing the fake SVX-tag template is that the distribution is symmetric. This assumption has been explicitly checked by combining tracks from separate back-to-back jets and constraining them to originate from a common vertex. The resulting pseudo-ct distribution is symmetric with respect to $ct = 0$ [27]. As an additional check, in Fig. 13 we compare the fake SVX-tag template derived from jet data with the distribution from a sample of generic Monte Carlo jets tagged by SECVTX. The Monte Carlo sample was obtained by running the tagging algorithm on gluon and light-quark jets generated in ISAJET. We did not require a μ tag in addition to the SVX tag, as the acceptance for this process is too small to simulate in a reasonable time. The comparison shows some disagreement near $ct = 0$. However, replacing the jet-data template with the Monte Carlo template and refitting the data, we find signal fractions of 0.806 ± 0.059 and 0.613 ± 0.017 for the forward and central data, respectively. These results are in excellent agreement with the fits using the jet-data template.

As a final check on the pseudo-ct fit, we use the mass M of the secondary vertex in place of ct and refit the data. The mass and pseudo-ct variables are largely uncorrelated and represent independent estimators of the b purity of the SVX tag. We use the same generic Monte Carlo sample described above to obtain the shape of the fake SVX-tag mass distribution. The bottom and charm templates come from the same samples used to obtain the pseudo-ct templates. We find that the fit cannot independently separate the charm and fake components. We therefore fix the relative contribution of charm and fake SVX tags to the result obtained using ct. With this constraint, the fitted $b\bar{b}$ fractions are 0.767 ± 0.051 and 0.616 ± 0.017 for the forward and central fits, respectively, which are consistent with the results using pseudo-ct. The mass fits are displayed in Fig. 14.

Because $p_T^{\rm rel}$ cannot separate muons from charm and light-quark decay, the charm template is used to represent both components in the fits. This choice is somewhat arbitrary, so as a check we substitute the decay-in-flight template and refit the data. We find $b\bar{b}$ fractions of 0.822 ± 0.056 and 0.658 ± 0.015 in the forward and central samples, respectively. The forward result is consistent with the fit using the charm $p_T^{\rm rel}$ template, but there is a systematic shift in the central sample. The relative difference in the ratio of $b\bar{b}$ events from the nominal fit is -5.4%, and we include this as a systematic uncertainty on the cross section ratio.

Finally, as a check on the Monte Carlo smearing procedure we refit the central data using a definition of $p_T^{\rm rel}$ based on tracking, rather than calorimeter, information.

The track clustering algorithm is similar to the jet clustering algorithm with tracks replacing calorimeter towers. The μ jet is unambiguously selected as the jet containing the muon track, and we calculate $p_T^{\rm rel}$ after subtracting the muon momentum vector from the jet. The fit result using this definition of $p_T^{\rm rel}$ is displayed in Fig. 15. The $b\bar{b}$ fraction is 0.641 ± 0.014, which is 3.9% higher than the nominal fit. We combine the resulting -3.9% shift in the cross section ratio with the -5.4% systematic uncertainty due to using the decay-in-flight $p_T^{\rm rel}$ template, and assign a total systematic uncertainty of -6.7% on the measured cross section ratio due to uncertainty in the fitted number of $b\bar{b}$ events.

VI. CROSS SECTION RATIO AND COMPARISON WITH QCD

The measured cross section ratio $R_{\rm expt}$ is defined and calculated with the following formula,

$$R_{\rm expt} = \frac{\sigma(p\bar{p} \to b_1 b_2 X; 2.0 < |y_{b_1}| < 2.6)}{\sigma(p\bar{p} \to b_1 b_2 X; |y_{b_1}| < 0.6)} = \frac{N_{b\bar{b}}^{\rm f}}{N_{b\bar{b}}^{\rm c}} \frac{\epsilon_{\rm c}}{\epsilon_{\rm f}}, \quad (3)$$

where $p_T(b_1)$, $p_T(b_2) > 25\,{\rm GeV}/c$, $|y_{b_2}| < 1.5$, and $\Delta\phi(b_1, b_2) > 60^\circ$ for both cross sections, $N_{b\bar{b}}^{\rm f(c)}$ are the number of background subtracted $b\bar{b}$ events in the forward (central) datasets, and $\epsilon_{\rm f(c)}$ are the total efficiencies. Combining the results of Sections IV and V, we find $R_{\rm expt} = 0.361 \pm 0.033$, where the error is statistical only.

A. Systematic Uncertainties

The primary motivation for presenting the ratio of forward and central $b\bar{b}$ production, rather than absolute cross sections, is that many of the experimental uncertainties cancel; including the luminosity, the vertex $|z| < 30\,{\rm cm}$ requirement, the muon branching fraction, and the SECVTX b-tagging efficiency. The remaining uncertainties are either reduced or are small to begin with. In this section we describe the estimation of these uncertainties.

The uncertainty on the jet energy scale receives contributions from both the absolute and relative (η-dependent) corrections [39]. The main sources of uncertainty on the absolute E_T scale are calorimeter response, fragmentation, and underlying event. The combined systematic uncertainty for these effects is estimated to be 3.6% for corrected jet $E_T = 15\,{\rm GeV}/c$, decreasing with increasing E_T. Fluctuating the jet E_T cuts $\pm 3.6\%$ changes the event yield by $^{+9.2}_{-10}\%$ and $^{+7.8}_{-7.3}\%$ in the forward and central samples, respectively. The resulting shift in $R_{\rm expt}$ is $^{+1.4}_{-3.2}\%$. Uncertainty on the relative jet energy correction arises from finite statistics in the dijet balancing analysis. Since the correction, and the uncertainty, depends on η_D, the effect of this uncertainty is determined by fluctuating the E_T correction for all jets $\pm 1\sigma$(stat) and observing the change in event yield. We find the relative change in the number of events to be $^{+1.5}_{-0.5}\%$ in the forward data, and $\pm 0.6\%$ in the central data. The resulting change in $R_{\rm expt}$ is $+1.0\%$.

We use the value 0.006 ± 0.002 for the Peterson fragmentation parameter. Fluctuating ϵ within this uncertainty changes the acceptance by $^{+10}_{-7.2}\%$ and $^{+7.4}_{-7.6}\%$ for the forward and central samples, respectively. The net shift in $R_{\rm expt}$ is -2.7%. However, more recent experimental studies by the OPAL [40] and ALEPH [41] collaborations at LEP favor a value of ϵ closer to 0.003, and a theoretical study [42] using NLO evolution for the perturbative part of the fragmentation function obtained $\epsilon = 0.0015 \pm 0.0002$ using $\Lambda_5 = 200\,{\rm MeV}$. For future comparison with different theoretical results, we have evaluated the acceptance taking the limit $\epsilon \to 0$. We find individual shifts of $+78\%$ and $+52\%$ for the forward and central acceptance, respectively. This results in a -15% shift in $R_{\rm expt}$, which can be taken as the maximum range of uncertainty due to fragmentation effects.

The systematic uncertainty on the CTC tracking efficiency takes into account variations with instantaneous luminosity and single-hit efficiency degradation in the inner superlayers over the course of Run 1B. The combined uncertainty from these effects is estimated to be $\pm 3.3\%$.

The uncertainty on the CMUP acceptance calculation was estimated by fluctuating the trigger efficiency parameters within their statistical uncertainties. The resulting systematic uncertainty is $\pm 1.7\%$.

Finally, in Sec. IV A the uncertainty on the FMU level 3 occupancy cut was determined to be $\pm 0.6\%$ by fluctuating the fitted slope within its uncertainty, and the consistency checks in Sec. V C resulted in an estimated uncertainty of -6.7% on $R_{\rm expt}$ due to uncertainty on the fitted number of $b\bar{b}$ events. Table IV summarizes the various sources of systematic uncertainty on $R_{\rm expt}$. Adding the individual uncertainties in quadrature results in a total systematic uncertainty of $^{+4.1}_{-8.7}\%$. The final value for the measured cross section ratio is $R_{\rm expt} = 0.361 \pm 0.033\,({\rm stat})^{+0.015}_{-0.031}\,({\rm syst})$.

B. Comparison with Theory

We compare our result to the NLO QCD calculation of Ref. [11] using MRSA′ PDFs, $m_b = 4.75\,{\rm GeV}/c^2$, and renormalization/factorization scale $\mu_0 = \sqrt{m_b^2 + \langle p_T \rangle^2}$, where $\langle p_T \rangle = \frac{1}{2}(p_T^b + p_T^{\bar{b}})$. In calculating the theoretical result $R_{\rm theor}$, the same p_T and rapidity cuts used in the acceptance calculation are applied. We find $R_{\rm theor} = 0.338^{+0.014}_{-0.097}$, in good agreement with the experimental result. The uncertainty was estimated by changing the scale factor between $2\mu_0$ and $\mu_0/2$.

In Fig. 16, we compare the experimental measurement to the predicted shape of $R = \sigma(y_{b_1})/\sigma(|y_{b_1}| < 0.6)$ as a function of y_{b_1}, integrated over rapidity bins of width

0.6 and normalized to the central bin. To illustrate that the b-quark rapidity distribution does not change significantly between LO and NLO, the Born cross section is shown as a dashed line in each bin. Due to the strong rapidity correlation between the b and $\bar{b}$, the predicted $d\sigma/dy_{b_1}$ distribution falls off rapidly once the trigger b is detected outside the rapidity range occupied by the second b ($|y_{b_2}| < 1.5$). The good agreement between experiment and theory is the first direct evidence that the rapidity correlation predicted by QCD is correct.

As mentioned in Sec. I, the shape of the rapidity distribution at large y is sensitive to the gluon distribution in the proton at large x. Assuming leading order ($2 \to 2$) kinematics, the range of x values probed by this measurement can be estimated using the following equations,

$$x_1 = \frac{M_T}{\sqrt{s}} \left[e^{+y_b} + e^{+y_{\bar{b}}} \right] \tag{4}$$

$$x_2 = \frac{M_T}{\sqrt{s}} \left[e^{-y_b} + e^{-y_{\bar{b}}} \right] \tag{5}$$

where $M_T = \sqrt{m_b^2 + p_T^2}$, and $\sqrt{s}$ is the center-of-mass energy of the colliding hadrons. In Fig. 17, we plot the fraction of proton momentum carried by the colliding partons in ISAJET forward-central $b\bar{b}$ events satisfying our cross section definition, where the x values were calculated using the generated b and $\bar{b}$ rapidities. The initial-state parton traveling in the direction of the forward b quark has momentum in the range $0.1 < x < 0.7$, while the second parton has momentum in the range $0.005 < x < 0.1$. Thus, the measurement is sensitive to $G(x, Q^2)$ in the region where it is not currently well constrained ($x > 0.15$).

In Fig. 18, we show the gluon-gluon luminosity $G(x_1)G(x_2)$ as a function of y_b for a representative set of PDFs: MRSR2 (dashed) [43], CTEQ4HJ (dotted) [44], and MRST (dot-dash) [45], all normalized to the MRSA′ gluon distribution. The approximate correspondence between the momentum fraction of the high-x parton and the rapidity of the forward b quark is facilitated by setting $y_{\bar{b}} = 0$ and $Q = 40\,\mathrm{GeV}$ in Eqs. 4 and 5, where the Q value is approximated by the mean p_T of b quarks in our data as determined by ISAJET. To simulate the cross section ratio measurement, all of the curves are normalized to unity at $y_b = 0$. The approximate region sampled by this measurement is indicated by the arrows.

The comparison in Fig. 18 shows significant differences between the various gluon parameterizations, which arise from the different constraints used in the global fits. The MRSR2 PDFs are an updated version of the MRSA′ "best fit" parameterization, using more recent HERA data and a value of α_s more consistent with the world average (0.120), and there is little difference between the two gluon distributions. In contrast, the CTEQ4HJ gluon distribution was specifically designed to fit the high-E_T jet data measured by CDF using Run 1A (1992-1993) data [2]. The result is a rapid rise at high x, or equivalently, large rapidity. Since the total momentum carried by gluons is well constrained, the increase at large x must be accompanied by a decrease at lower momentum fraction, which happens to occur in the region sampled by this measurement. The MRST parton set represents the first systematic attempt to include k_T smearing when fitting prompt photon data as part of a global parton distribution analysis. They obtain three different parameterizations corresponding to a range of $\langle k_T \rangle$ from 0.0 to a maximum value consistent with data. Since a larger $\langle k_T \rangle$ is compensated by a smaller gluon distribution, the three parameterizations are referred to as MRST($g \uparrow$), MRST, and MRST($g \downarrow$). We show in Fig. 18 the MRST gluon distribution, which is significantly smaller than MRSA′ in the region dominated by prompt photon data. The MRST($g \uparrow$) gluon distribution (not shown) includes no k_T smearing and is consistent with MRSA′, while MRST($g \downarrow$) is approximately 60% lower than MRSA′ at $y_b = 2.0$. The CTEQ4M [44] gluon distribution (not shown) is a best-fit parameterization similar to MRSA′ and MRSR2.

In Fig. 19, we compare the measured cross section ratio with the NLO QCD predictions using the PDFs described above. To better discern the differences between the various theory curves, we present the results in the format data/theory, where our data point and the theory curves are divided by the result using MRSA′. The vertical error bars at the end of each theory curve indicate the statistical uncertainty from the Monte Carlo integration; we do not include the variation with scale in this plot. The measurement error is combined statistical and systematic.

As suggested by the comparison in Fig. 18, we find good agreement between data and QCD using the MRSR2 PDFs, while the CTEQ4HJ and MRST results are lower by approximately 1.5 and 2.0σ, respectively, where σ is the total error on the measurement. We note that taking the extreme value of Peterson ϵ ($= 0$) decreases R_{expt} by 15% (Sec. VI A), which would bring our result into agreement with the CTEQ4HJ prediction and within 1σ of the MRST result. We conclude that it would be premature to exclude either of these PDFs based on the comparison in Fig. 19. The current ambiguity on the exact shape of the non-perturbative b-quark fragmentation function limits the precision with which the gluon distribution can be constrained by this forward $b\bar{b}$ production measurement. However, this result does represent an independent constraint on the gluon distribution in a region of x where only a few measurements exist that are directly sensitive to $G(x, Q^2)$.

VII. SUMMARY

We have presented the first direct measurement of $b\bar{b}$ rapidity correlations at a hadron collider. Using forward and central high-p_T muon triggers, two independent sam-

ples were accumulated corresponding to events enriched in forward and central b decays, respectively. In each sample a secondary vertex b-tagging algorithm was used to identify a central recoil jet likely to contain a heavy quark. The fraction of events in each sample due to $b\bar{b}$ production was determined by simultaneously fitting $p_T^{\rm rel}$ between the muon and μ jet, and the transverse decay length of the b-tagged jets.

We have measured the ratio of forward-central to central-central $b\bar{b}$ production and find $R_{\rm expt} = 0.361 \pm 0.033^{+0.015}_{-0.031}$, where the first uncertainty is statistical and the second is systematic. This result is in good agreement with the NLO QCD prediction using MRSA′ PDFs, $R_{\rm theor} = 0.338^{+0.014}_{-0.097}$, and represents the first direct experimental evidence consistent with the strong $b\bar{b}$ rapidity correlation predicted by theory. A comparison with the QCD result using MRSR2 also shows good agreement, while the predictions using CTEQ4HJ and MRST indicate reasonable agreement within the large (15%) estimated uncertainty due to ambiguity in the exact shape of the b-quark fragmentation function. This uncertainty is comparable to the current variation in the gluon distribution due to the uncertainty in parameterizing initial-state k_T smearing when analyzing prompt photon data. Given the small number of measurements directly sensitive to the gluon distribution at high x, this result represents an important additional constraint that could reduce the range of possible gluon parameterizations if it is incorporated into the global analyses.

ACKNOWLEDGMENTS

We thank the Fermilab staff and the technical staff at the participating institutions for their essential contributions to this research. This work is supported by the U.S. Department of Energy and the National Science Foundation; the Natural Sciences and Engineering Research Council of Canada; the Istituto Nazionale di Fisica Nucleare of Italy; the Ministry of Education, Science and Culture of Japan; the National Science Council of the Republic of China; and the A. P. Sloan Foundation.

[1] E. L. Berger, Phys. Rev. D **37**, 1810 (1988).
[2] F. Abe *et al.*, The CDF Collaboration, Phys. Rev. Lett. **77**, 438 (1996).
[3] H. L. Lai *et al.*, The CTEQ Collaboration, Phys. Rev. D **55**, 1280 (1997), and references therein.
[4] J. Huston *et al.*, The CTEQ Collaboration, **hep-ph**/9801444 (1998), submitted to Phys. Rev. D.
[5] J. Huston *et al.*, the CTEQ Collaboration, Phys. Rev. D **51**, 6139 (1995).
[6] L. Apanasevich *et al.*, The E706 Collaboration, **hep-ex**/9808467 (1998).
[7] C. Albajar *et al.*, The UA1 Collaboration, Z. Phys. C **61**, 41 (1994); Phys. Lett. B **256**, 121 (1991).
[8] F. Abe *et al.*, The CDF Collaboration, Phys. Rev. D **47**, 2639 (1993); Phys. Rev. Lett. **75**, 1451 (1995); Phys. Rev. D **53**, 1051 (1996); Phys. Rev. D **55**, 2546 (1997).
[9] S. Abachi *et al.*, The DØ Collaboration, Phys. Rev. Lett. **74**, 2422 (1995).
[10] S. Abachi *et al.*, The DØ Collaboration, submitted to the Int. Conf. on High Energy Physics, Warsaw, 1996.
[11] M. Mangano, P. Nason, and G. Ridolfi, Nucl. Phys. B **373**, 295 (1992).
[12] S. Frixione *et al.*, **hep-ph**/9702287 (1997), to appear in *Heavy Flavours II*, A. J. Buras and M. Lindner, Advanced Series on Directions in High-Energy Physics, World Scientific, Singapore (1997).
[13] M. Mangano, **hep-ph**/9711337 (1997).
[14] F. I. Olness, R. J. Scalise, and Wu-Ki Tung, **hep-ph**/9712494 (1997).
[15] F. Abe *et al.*, The CDF Collaboration, Nucl. Instrum. Methods A **271**, 387 (1988), and references therein.
[16] D. Amidei *et al.*, Nucl. Instrum. Methods A **350**, 73 (1994);
[17] P. Azzi *et al.*, Nucl. Instrum. Methods A **360**, 137 (1995).
[18] F. Bedeschi *et al.*, Nucl. Instrum. Methods A **268**, 51 (1988).
[19] G. Ascoli *et al.*, Nucl. Instrum. Methods A **268**, 33 (1988).
[20] K. Byrum *et al*, Nucl. Instrum. Methods A **268**, 46 (1988)
[21] L. Balka *et al.*, Nucl. Instrum. Methods A **267**, 272 (1988); S. Bertolucci *et al.*, Nucl. Instrum. Methods A **267**, 301 (1988); Y. Fukui *et al.*, Nucl. Instrum. Methods A **267**, 280 (1988); G. Brandenburg *et al.*, Nucl. Instrum. Methods A **267**, 257 (1988); S. Cihangir *et al.*, Nucl. Instrum. Methods A **267**, 249 (1988).
[22] F. Abe *et al.*, The CDF Collaboration, Phys. Rev. D **45**, 1448 (1992).
[23] F. Abe *et al.*, The CDF Collaboration, Phys. Rev. D **47**, 4857 (1993).
[24] F. Abe *et al.*, The CDF Collaboration, Phys. Rev. Lett. **68**, 1104 (1992).
[25] D. Amidei *et al.*, Nucl. Instrum. Methods A **269**, 51 (1988); J. T. Carroll *et al.*, Nucl. Instrum. Methods A **263**, 199 (1988).
[26] G. W. Foster *et al.*, Nucl. Instrum. Methods A **269**, 93 (1988).
[27] F. Abe *et al.*, The CDF Collaboration, Phys. Rev. D **50**, 2966 (1994).
[28] F. Abe *et al.*, The CDF Collaboration, Phys. Rev. D **58**, 072001 (1998).
[29] A. Warburton, Ph.D. thesis, University of Toronto, 1997.
[30] F. Paige and S. D. Protopopescu, BNL Report No. 38034, 1986 (unpublished).
[31] A. Martin *et al.*, Phys. Lett. B **354**, 155 (1995).
[32] C. Peterson *et al.*, Phys. Rev. D **27**, 105 (1983).
[33] J. Chrin, Z. Phys. C **36**, 165 (1987); D. Buskulic *et al.*, The ALEPH Collaboration, Phys. Lett. B **244**, 551 (1990).
[34] P. Avery, K. Read, and G. Trahern, Cornell Internal Note

No. CSN-212, 1985 (unpublished).
[35] V. Barger, A. Stange, and R. Phillips, Phys. Rev. D **44**, 1987 (1991).
[36] J. Olsen, Ph.D. thesis, University of Wisconsin, 1998.
[37] F. Abe *et al.*, The CDF Collaboration, Phys. Rev. Lett. **76**, 3070 (1996).
[38] T. C. Caso *et al.*, Particle Data Group, Eur. Phys. J. C **3**, 1 (1998).
[39] F. Abe *et al.*, The CDF Collaboration, Phys. Rev. Lett. **70**, 1376 (1993).
[40] G. Alexander *et al.*, The OPAL Collaboration, Phys. Lett. B **364**, 93 (1995); Z. Phys. C **67**, 27 (1995).
[41] D. Buskulic *et al.*, The ALEPH Collaboration, Phys. Lett. B **357**, 699 (1995).
[42] M. Cacciari and M. Greco, Phys. Rev. D **55**, 7134 (1997).
[43] A. D. Martin, R. G. Roberts, and W. J. Stirling, Phys. Lett. B **387**, 419 (1996).
[44] H. L. Lai *et al.*, The CTEQ Collaboration, Phys. Rev. D **55**, 1280 (1997).
[45] A. D. Martin, R. G. Roberts, W. J. Stirling, and R. S. Thorne, Eur. Phys. J. C **4**, 463 (1998).

Forward Efficiency

Cut	Efficiency
Acceptance	$(7.73 \pm 0.09) \times 10^{-3}$
Level 1	0.714 ± 0.016
Splash Cut	0.885 ± 0.004
L3 Jet Cut	0.986 ± 0.003
C.L. (χ^2)	0.920 ± 0.010
Total Forward ϵ	$(4.43 \pm 0.12) \times 10^{-3}$

TABLE I. Summary of the total efficiency for the forward sample. Errors are statistical only.

Central Efficiency

Cut	Efficiency
Acceptance	$(2.54 \pm 0.06) \times 10^{-2}$
Muon ID	0.966 ± 0.004
Level 3	0.985 ± 0.010
Tracking	0.962 ± 0.009
Total Central ϵ	$(2.32 \pm 0.07) \times 10^{-2}$

TABLE II. Summary of the total efficiency for the central sample. Errors are statistical only.

Fit Results

Component	Forward Fit	Central Fit
f_{bb}	0.815 ± 0.060	0.617 ± 0.017
f_{cc}	0.083 ± 0.051	0.148 ± 0.014
f_{bf}	$0.000^{+0.059}_{-0.000}$	0.066 ± 0.021
f_{fb}	$0.017^{+0.047}_{-0.017}$	0.070 ± 0.010
f_{fc}	$0.086 \pm^{+0.035}_{-0.046}$	0.099 ± 0.010

TABLE III. Fitted fractions for each source in the forward and central fits. The first and second indices on the component symbols refer to the source of the SVX tag and μ tag, respectively. Fit errors correspond to a change in the log likelihood of 0.5.

Summary of Systematic Uncertainties

Source	Uncertainty (%)
Jet E_t scale (absolute)	$^{+1.4}_{-3.2}$
Jet E_t scale (relative)	$+1.0$
Fragmentation	-2.7
CTC tracking efficiency	± 3.3
CMUP trigger efficiency	± 1.7
FMU level 3 occupancy cut	± 0.6
Fitting procedure	-6.7
Total Uncertainty	$^{+4.1}_{-8.7}$

TABLE IV. Summary of systematic uncertainties on the cross section ratio. The total uncertainty is the quadrature sum of the individual uncertainties.

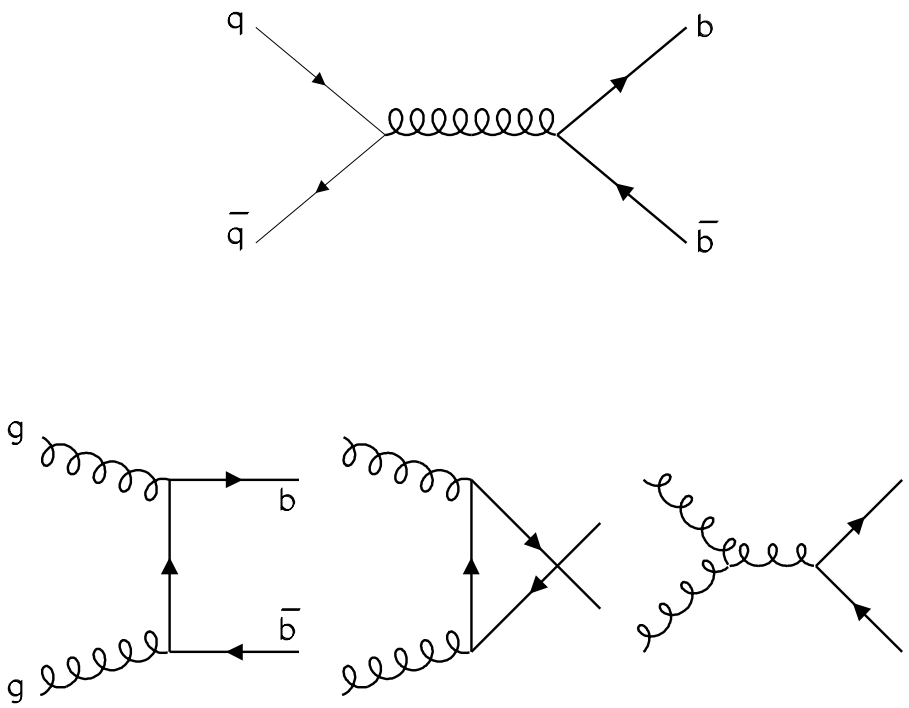

FIG. 1. Lowest order Feynman diagrams for $b\bar{b}$ production.

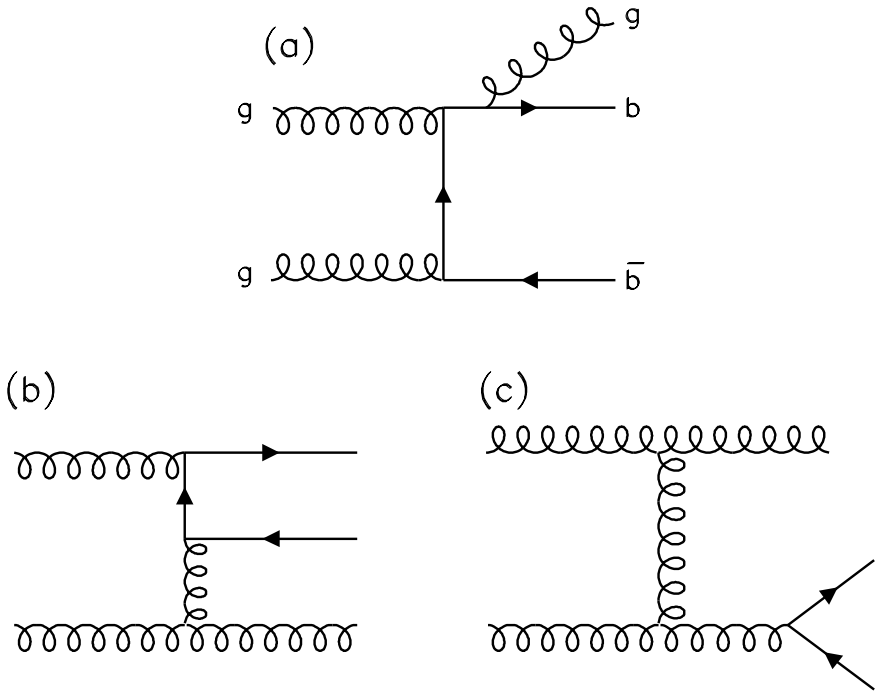

FIG. 2. Representative Feynman diagrams for the (a) direct, (b) flavor excitation, and (c) gluon splitting $b\bar{b}$ production processes.

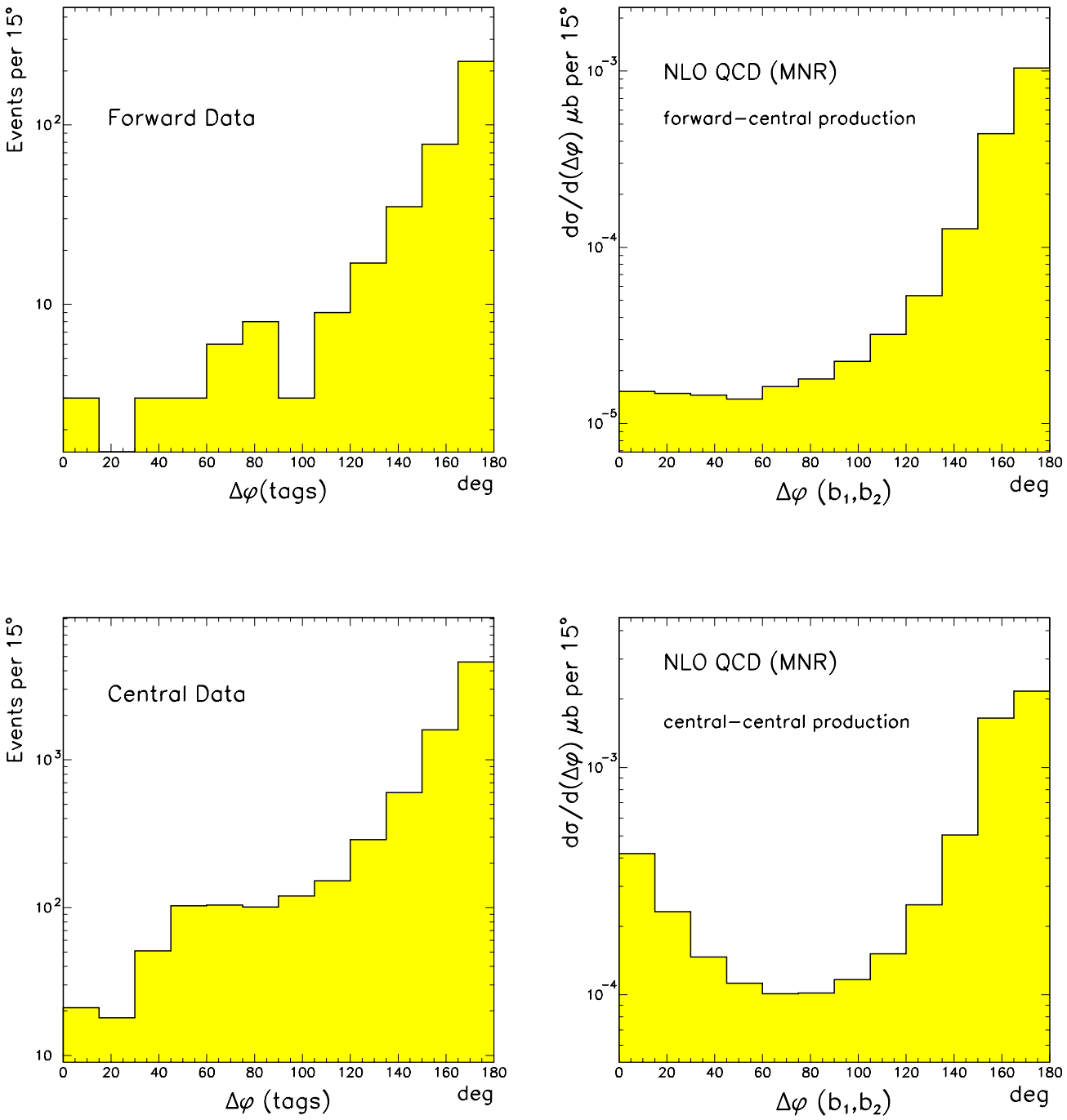

FIG. 3. The observed azimuthal opening angle between the μ tag and SVX tag in forward (top left) and central (bottom left) data events compared to the NLO QCD $\Delta\phi(b_1, b_2)$ distribution for the forward-central (top right) and central-central (bottom right) topologies.

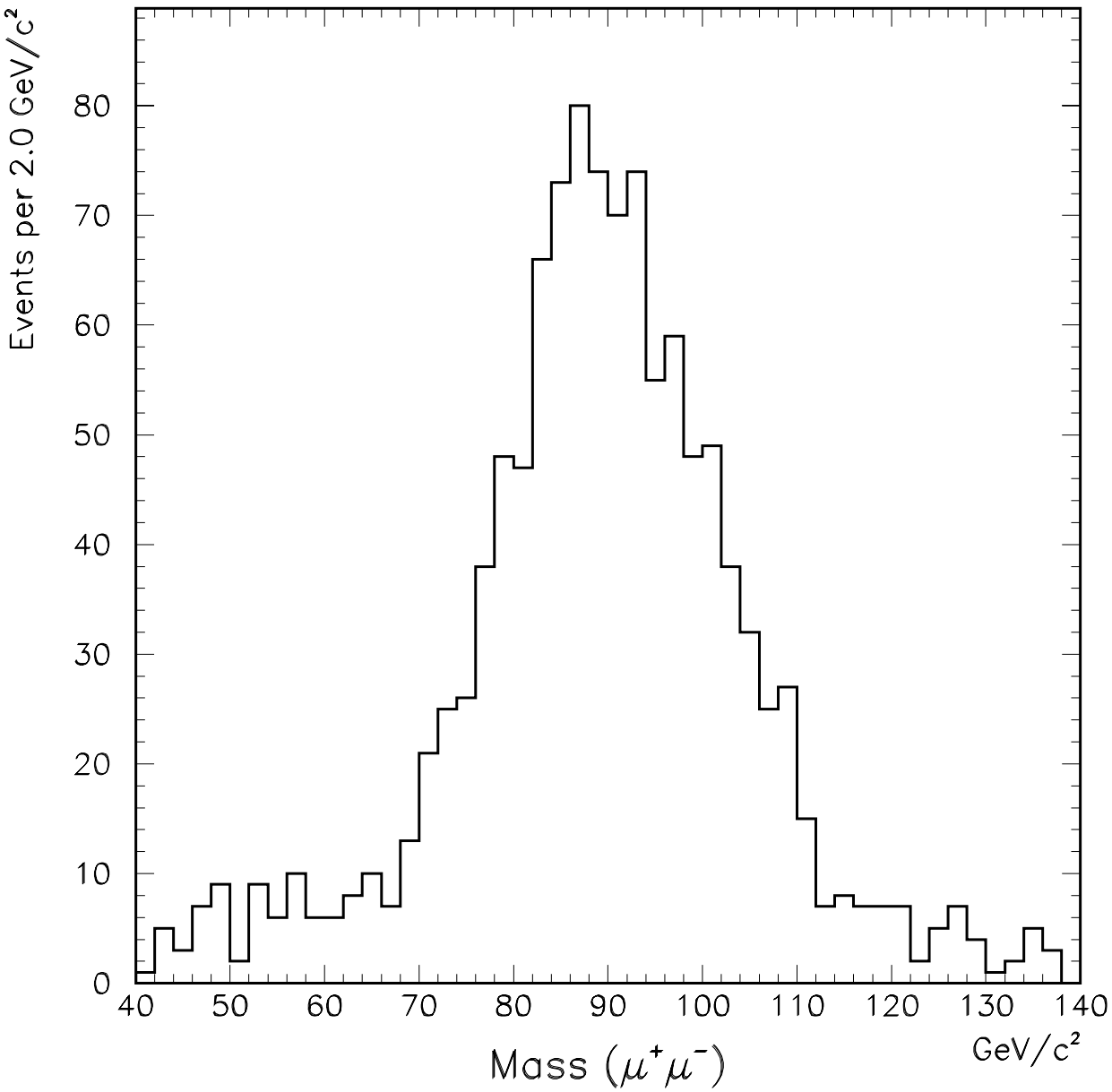

FIG. 4. Invariant mass distribution for the opposite charge FMU-CMU muon pairs used to measure the FMU detector efficiency.

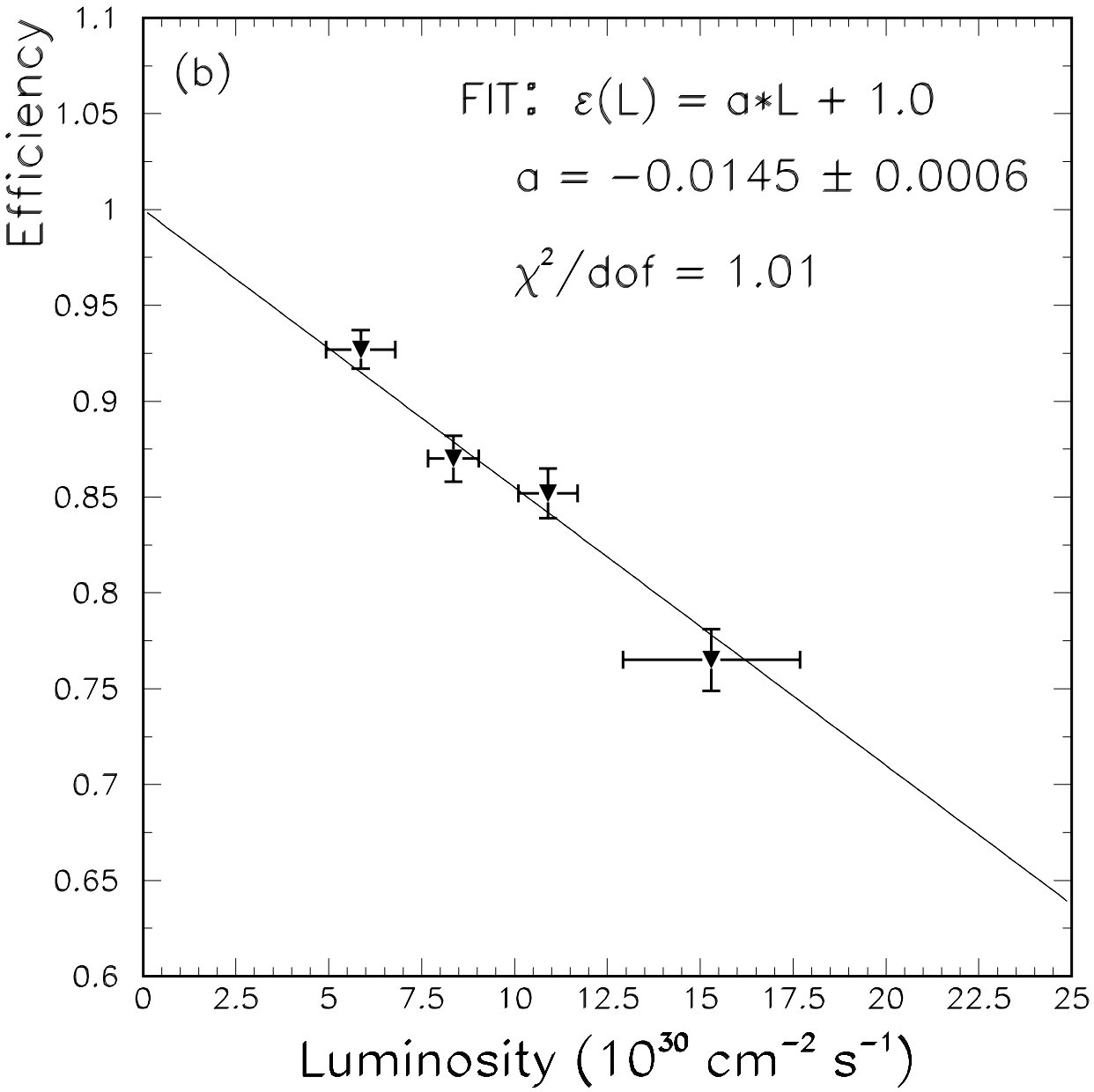

FIG. 5. Efficiency of the FMU level 3 occupancy cut as a function of instantaneous luminosity. Data points are plotted at the mean of four luminosity bins: $1.0 - 7.2$, $7.2 - 9.6$, $9.6 - 12.4$, > 12.4. Horizontal error bars correspond to the variance in each bin. The solid line is a linear fit to the data with the constraint $\epsilon(\mathcal{L} = 0) = 1.0$.

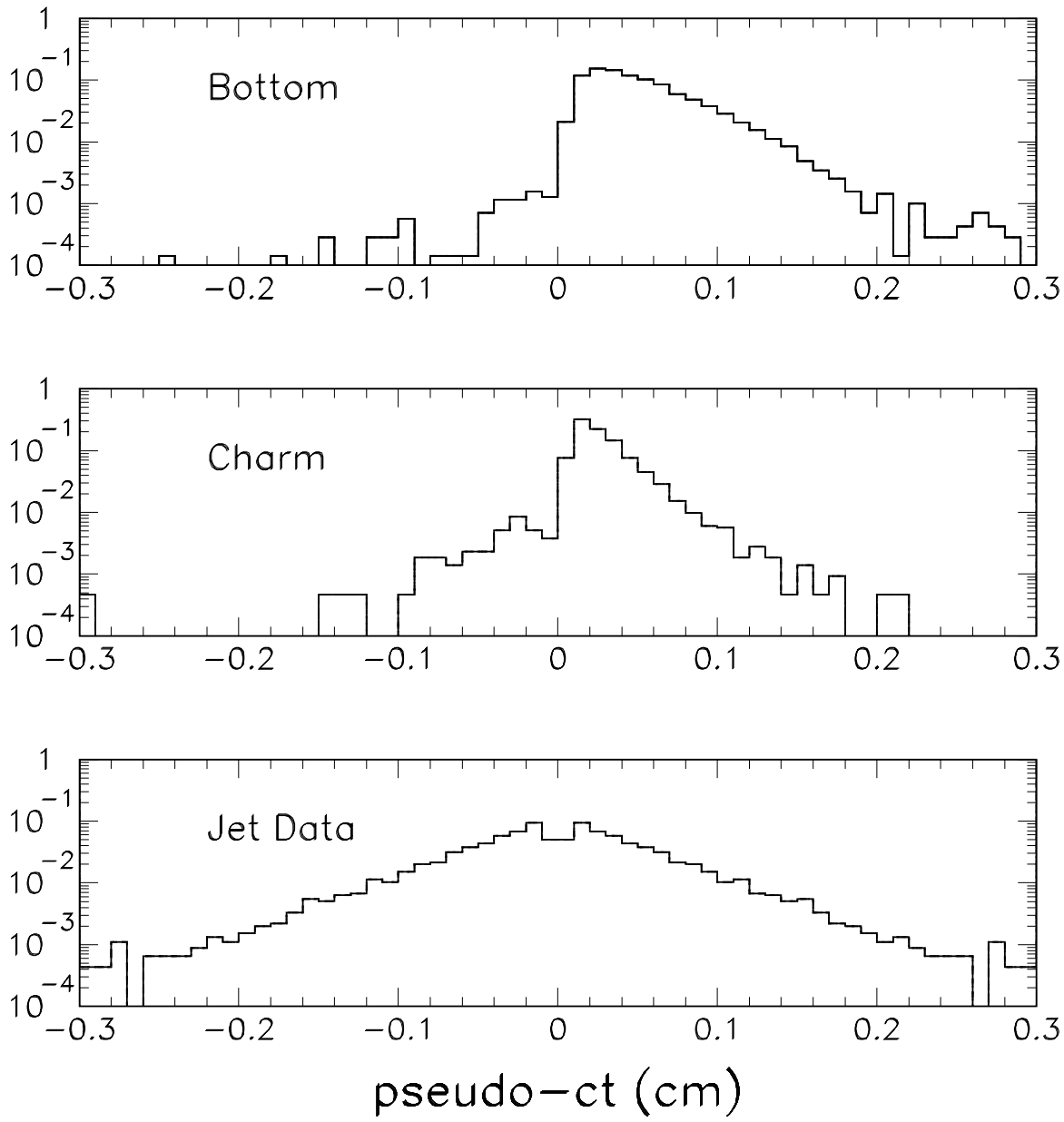

FIG. 6. Pseudo-ct distributions for the SVX tag in bottom and charm Monte Carlo, and for the symmetrized negative tags in jet data. The jet data shape is used as the fake-tag background template.

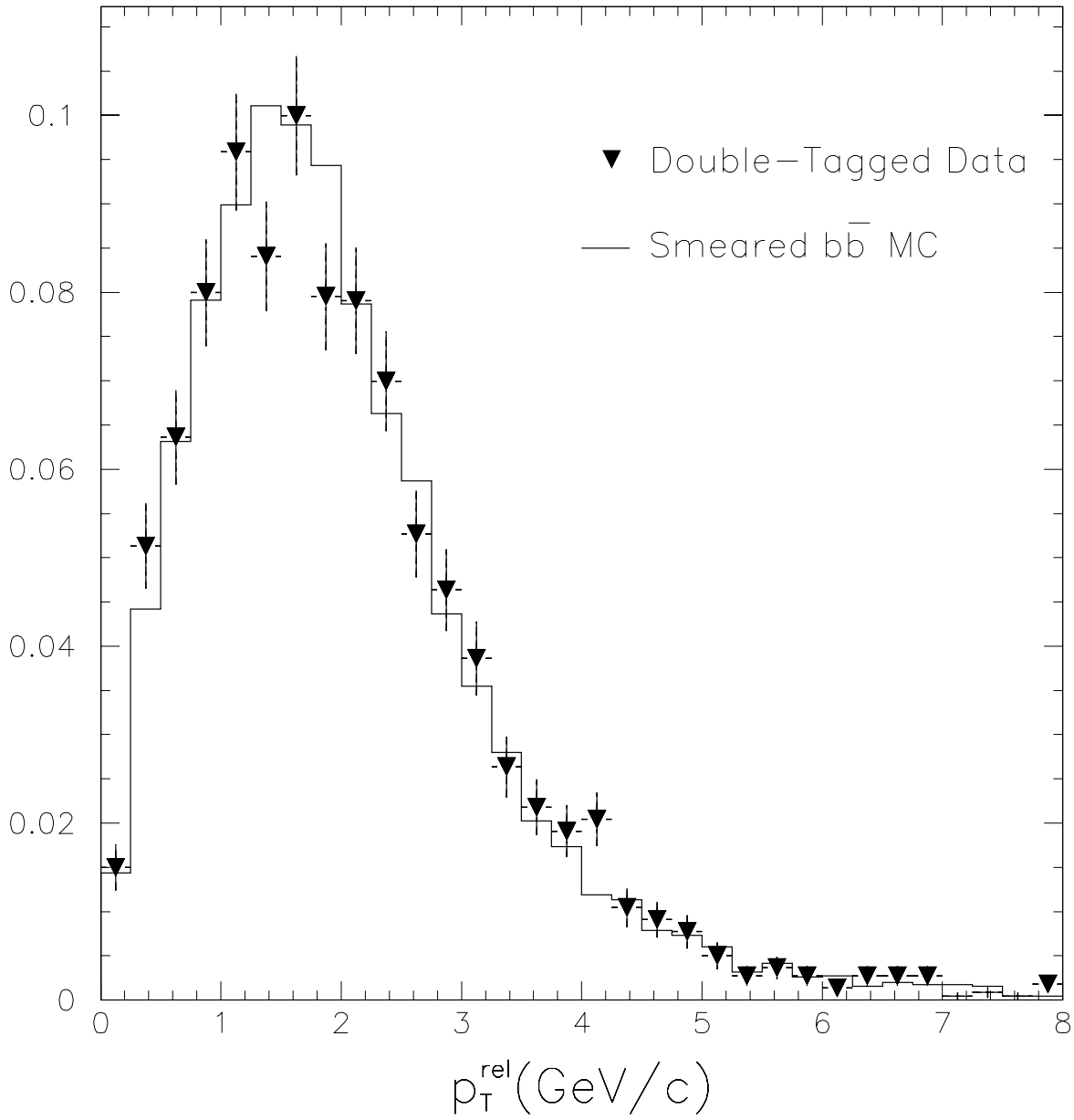

FIG. 7. The $b\bar{b}$ $p_T^{\rm rel}$ distribution from smeared Monte Carlo (hist) compared to the subset of central data events where the μ jet also contains a b tag (points).

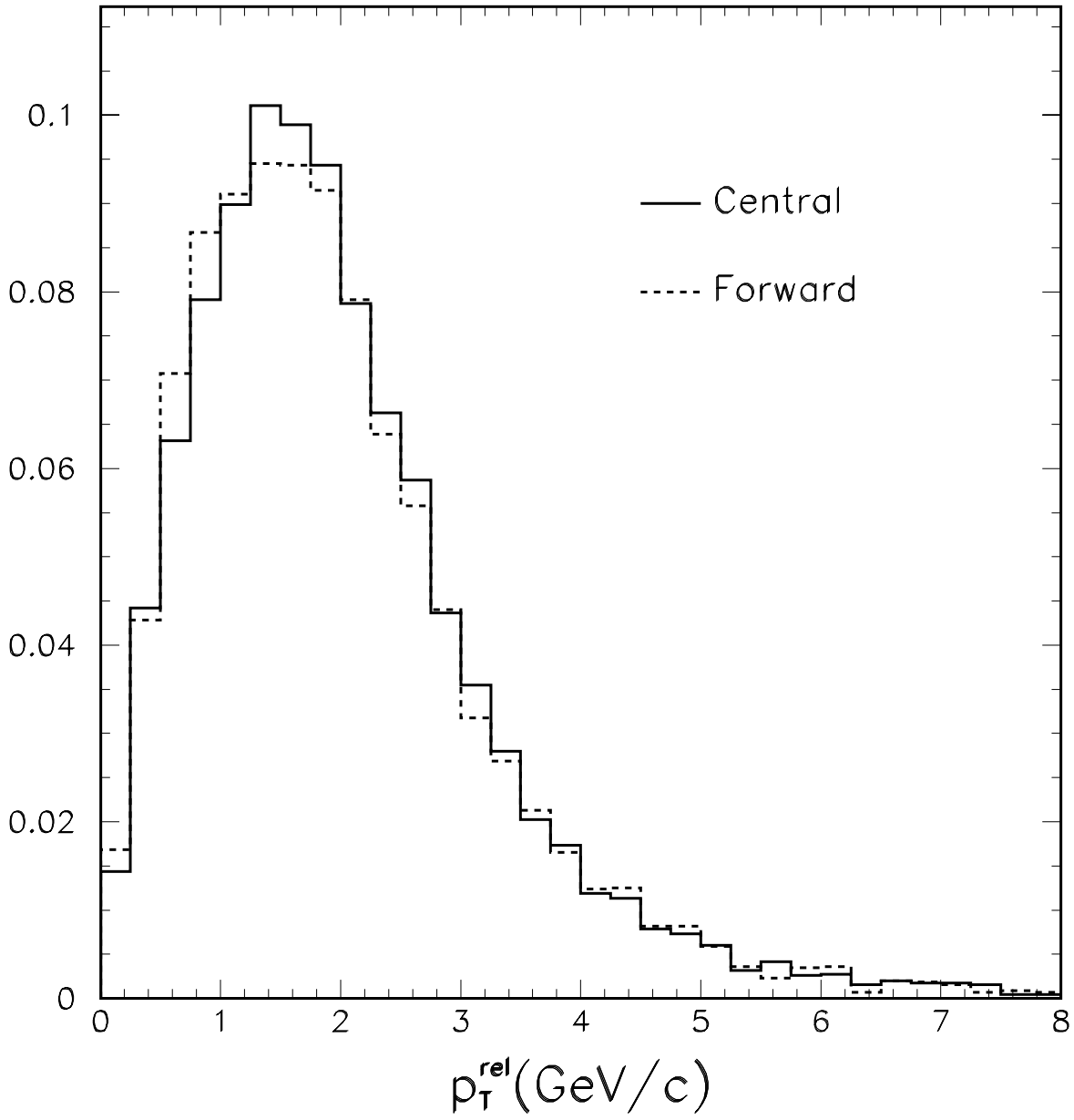

FIG. 8. Comparison of $p_T^{\rm rel}$ distributions in central (solid) and forward (dash) smeared $b\bar{b}$ Monte Carlo samples.

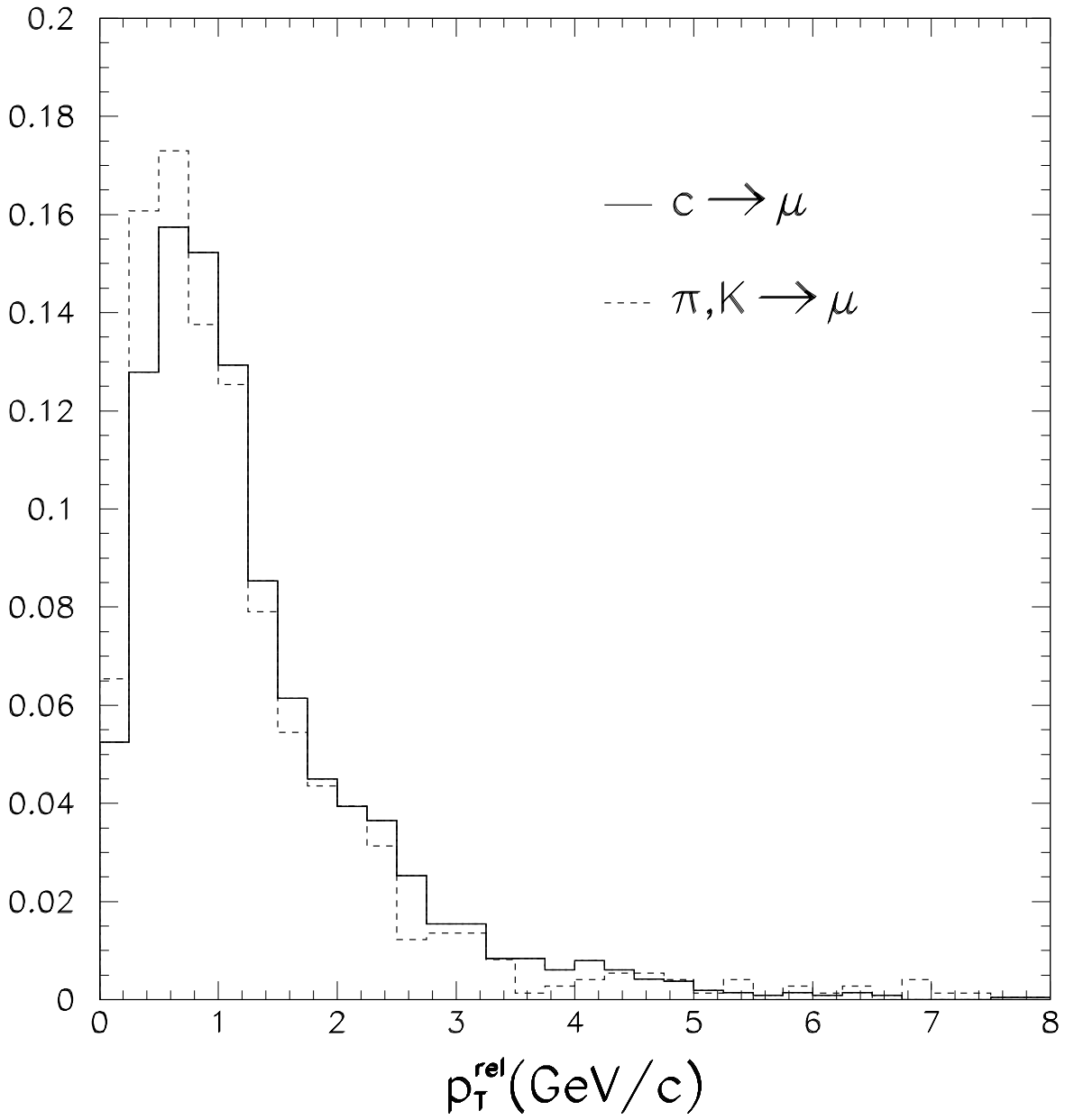

FIG. 9. Distributions of $p_T^{\rm rel}$ for forward muons from the decay of charm (solid), and light mesons (dashed) using smeared Monte Carlo.

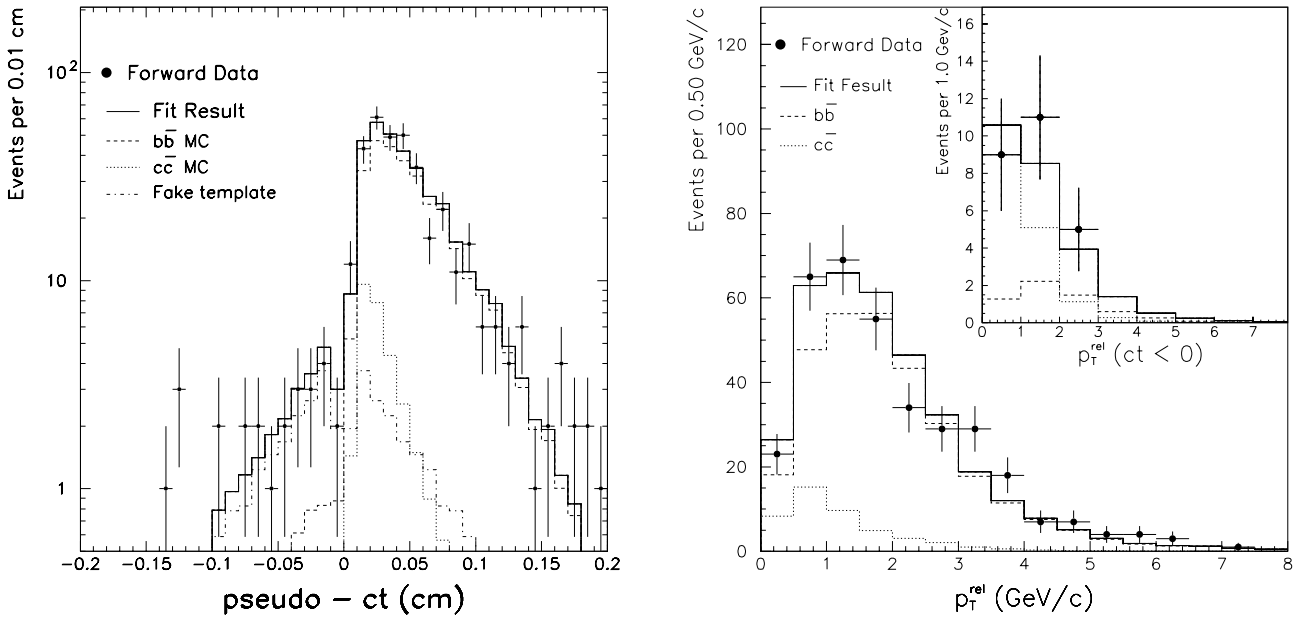

FIG. 10. Forward data fit result for pseudo-ct and $p_T^{\rm rel}$. The main $p_T^{\rm rel}$ plot shows the distribution for events with $ct > 0$, while the inset shows the events with $ct < 0$.

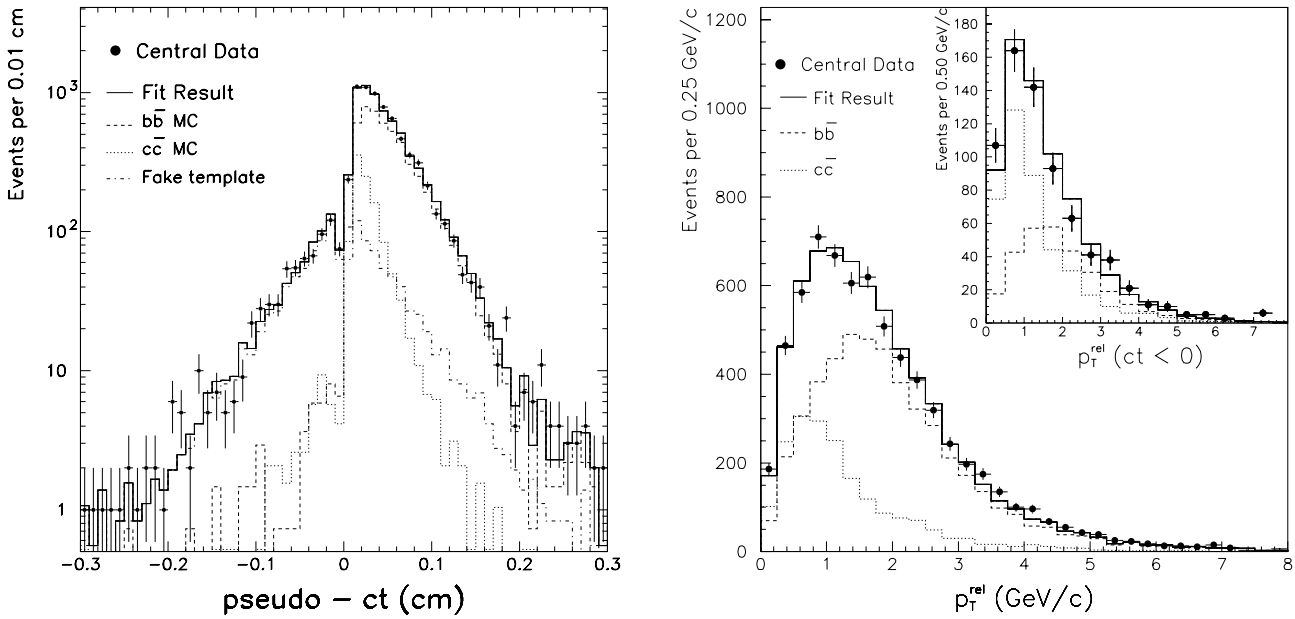

FIG. 11. Central data fit result for pseudo-ct and $p_T^{\rm rel}$. The main $p_T^{\rm rel}$ plot shows the distribution for events with $ct > 0$, while the inset shows the events with $ct < 0$.

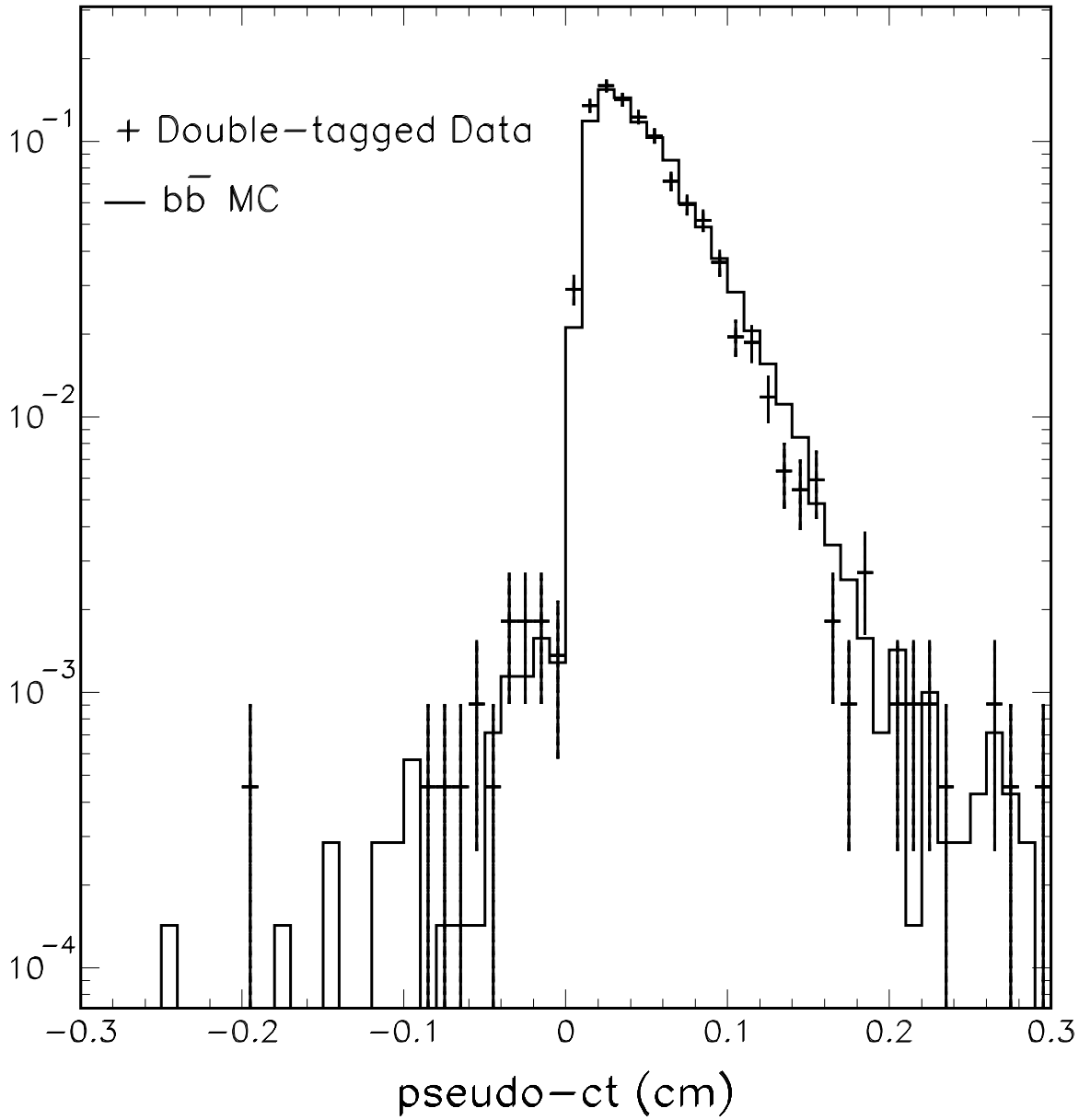

FIG. 12. Comparison between the $b\bar{b}$ pseudo-ct template and the distribution for SVX tags in the subset of central data events where the μ jet also contains a b tag.

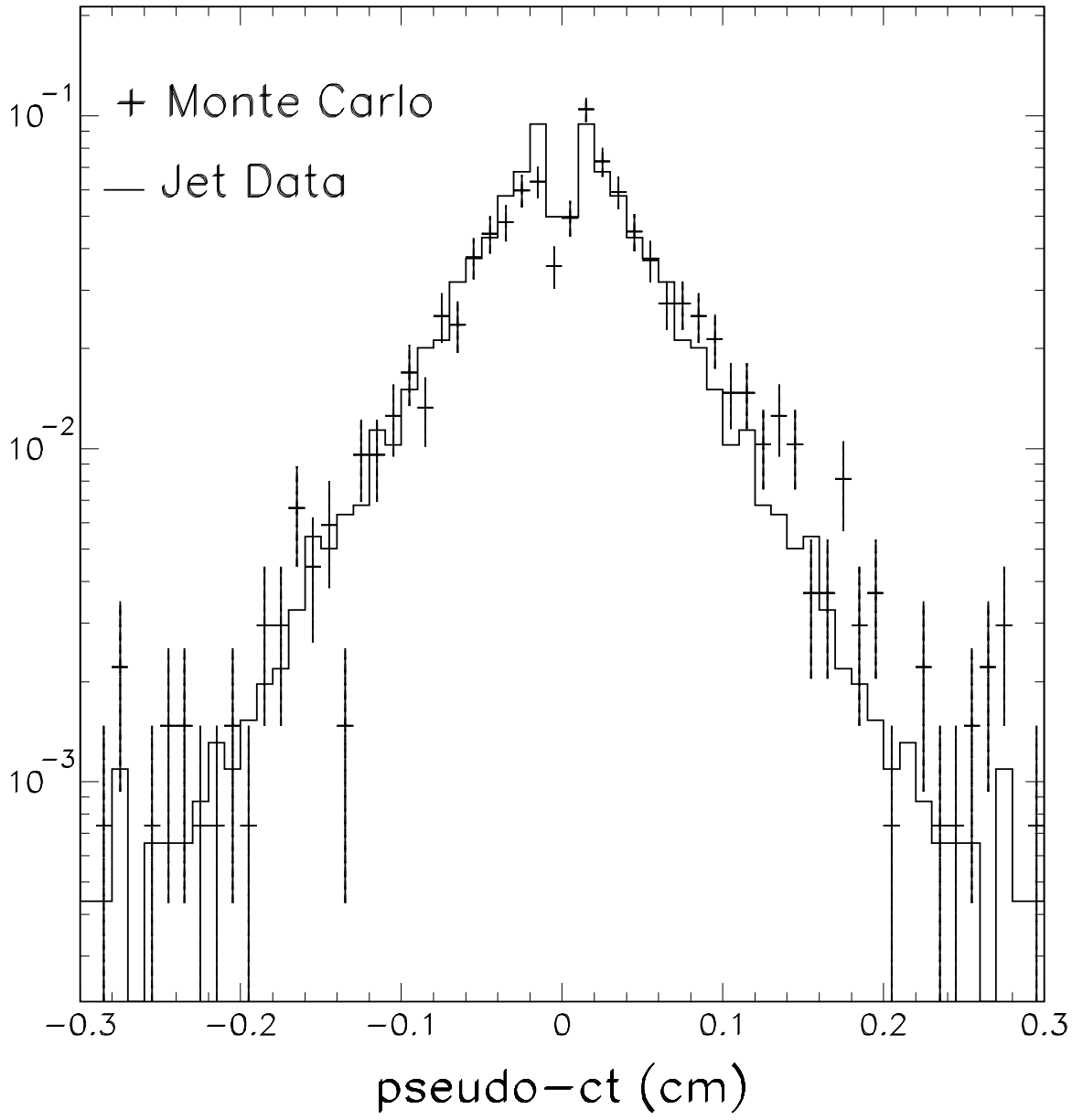

FIG. 13. The pseudo-ct distribution for Monte Carlo gluon and light-quark jets (points) compared to the fake template obtained by symmetrizing the negative pseudo-ct distribution in a sample of inclusive jets (histogram).

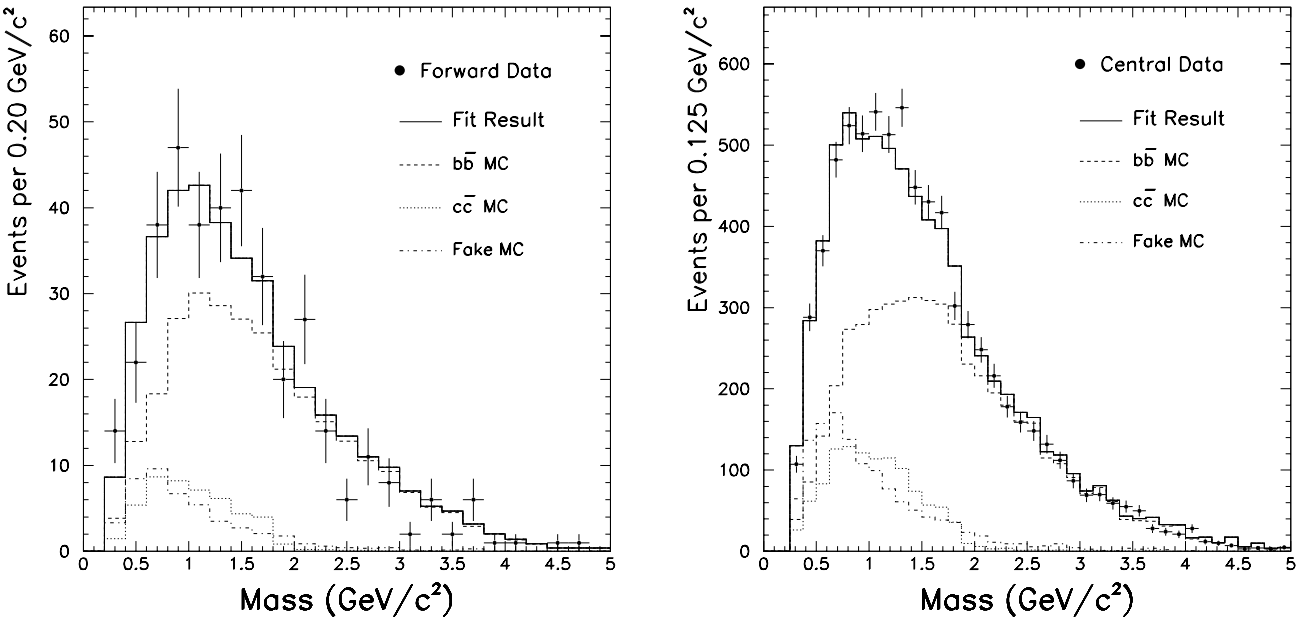

FIG. 14. Fit results for the forward (left) and central (right) data using the mass of the secondary vertex and $p_T^{\rm rel}$.

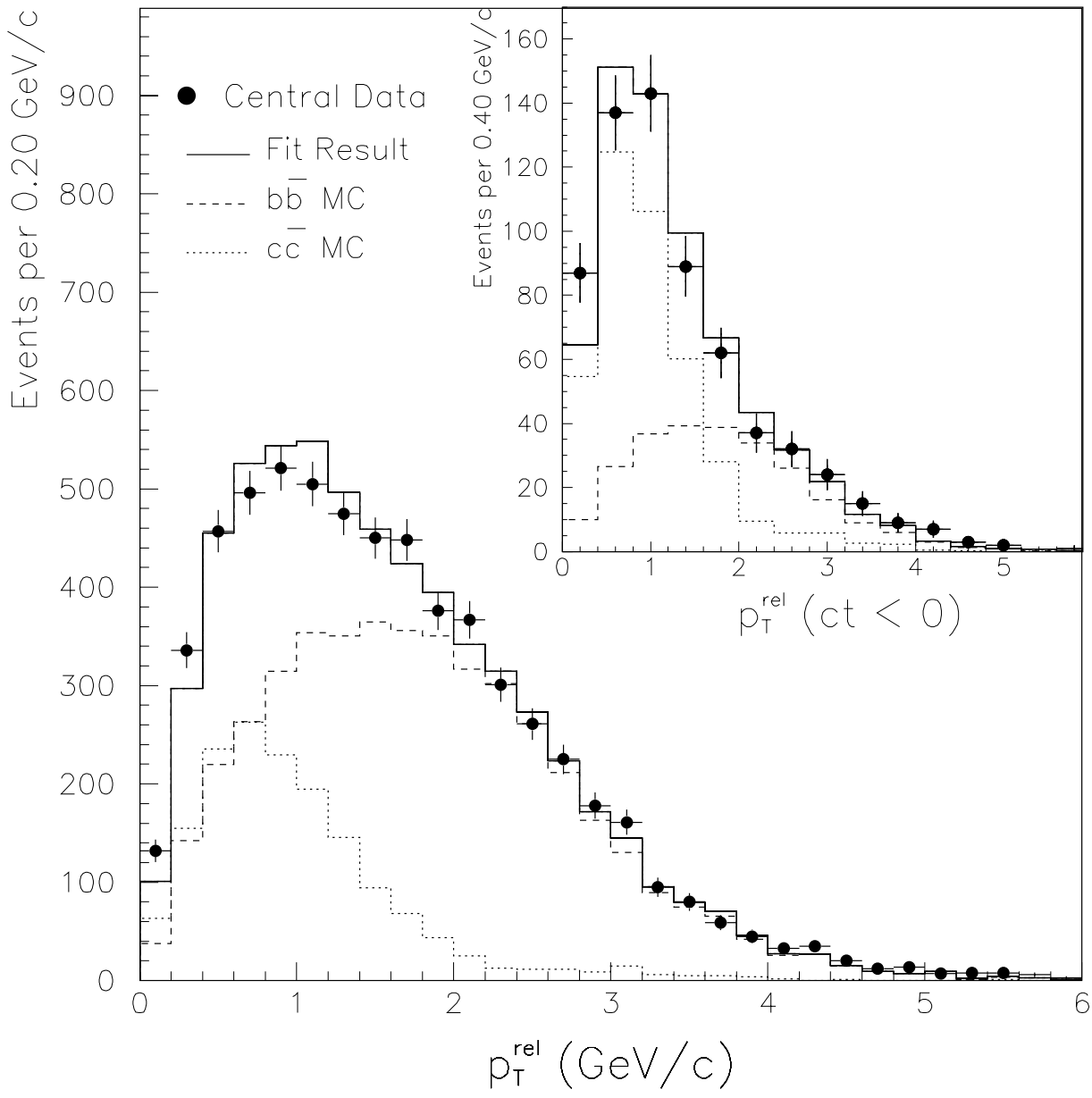

FIG. 15. Result of the central muon data fit using pseudo-ct and track-based $p_T^{\rm rel}$. Templates are from default Monte Carlo.

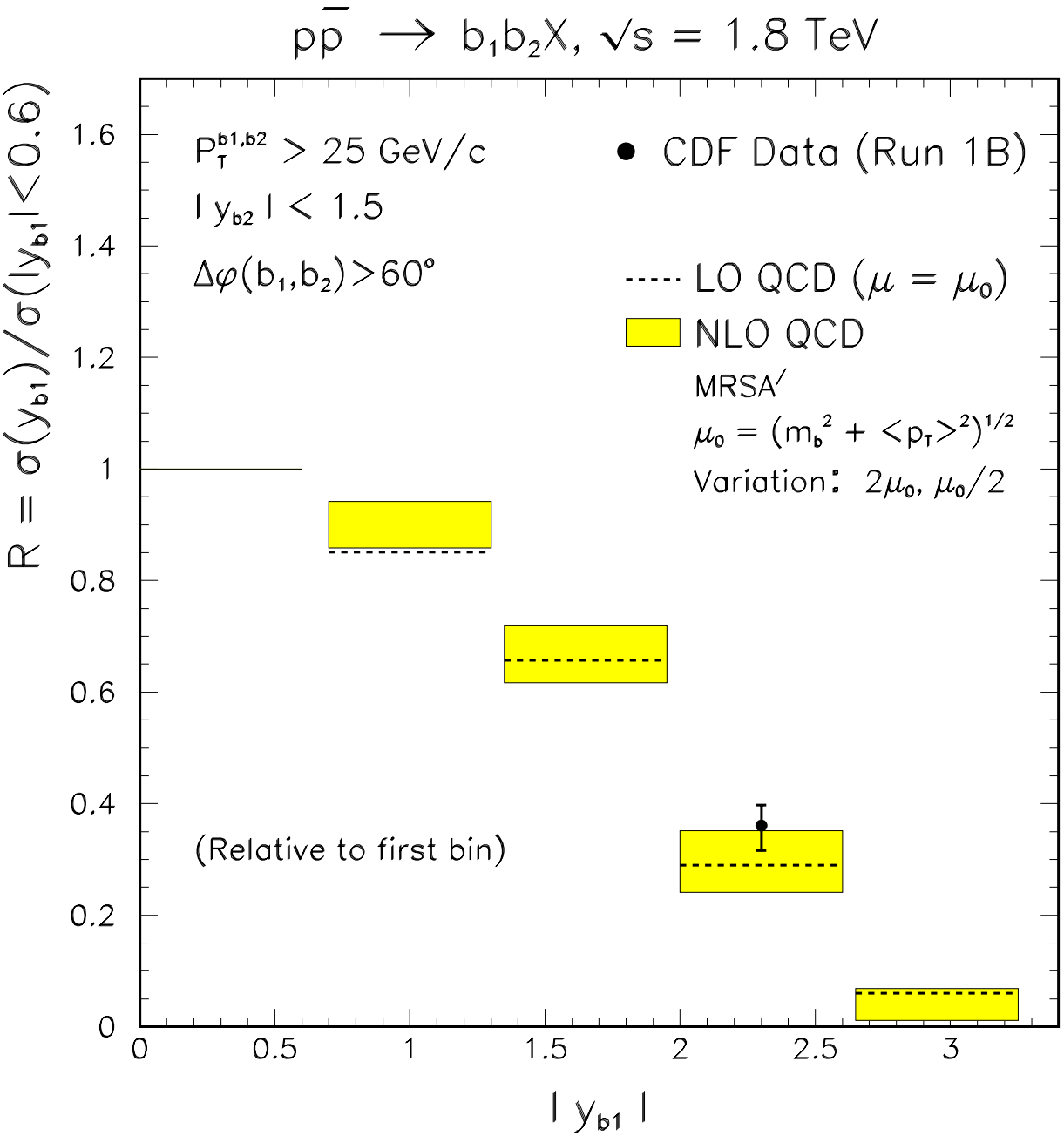

FIG. 16. The normalized rapidity distribution of the trigger b quark. Filled boxes are the theory prediction in each bin taking into account variations in the scale, the dashed line is the LO result, and the experimental measurement is indicated by the error bar.

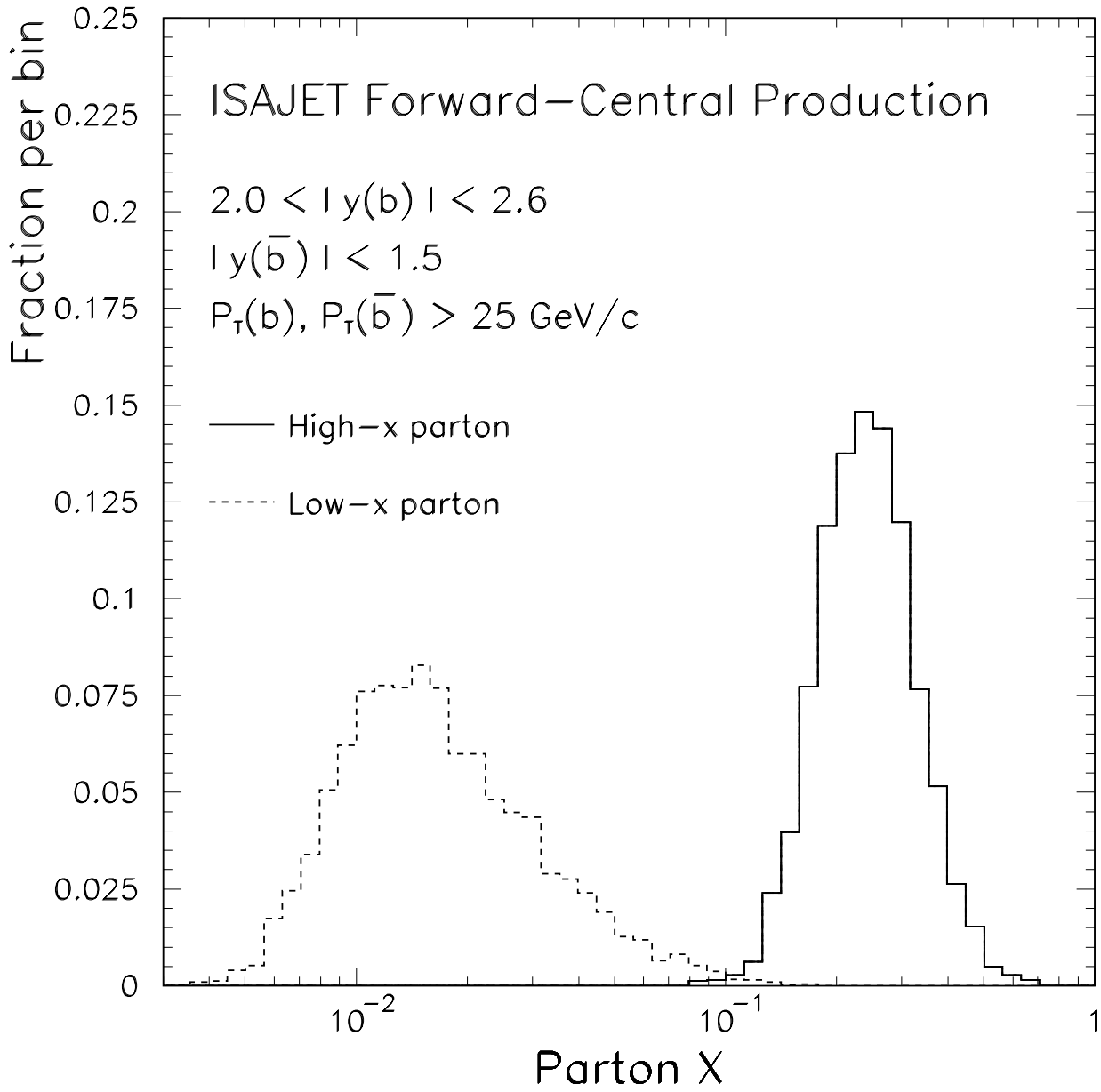

FIG. 17. The fraction of hadron momentum carried by the colliding partons in ISAJET forward-central $b\bar{b}$ production. The high-x parton corresponds to Eq. 4 (5) when y_b is positive (negative).

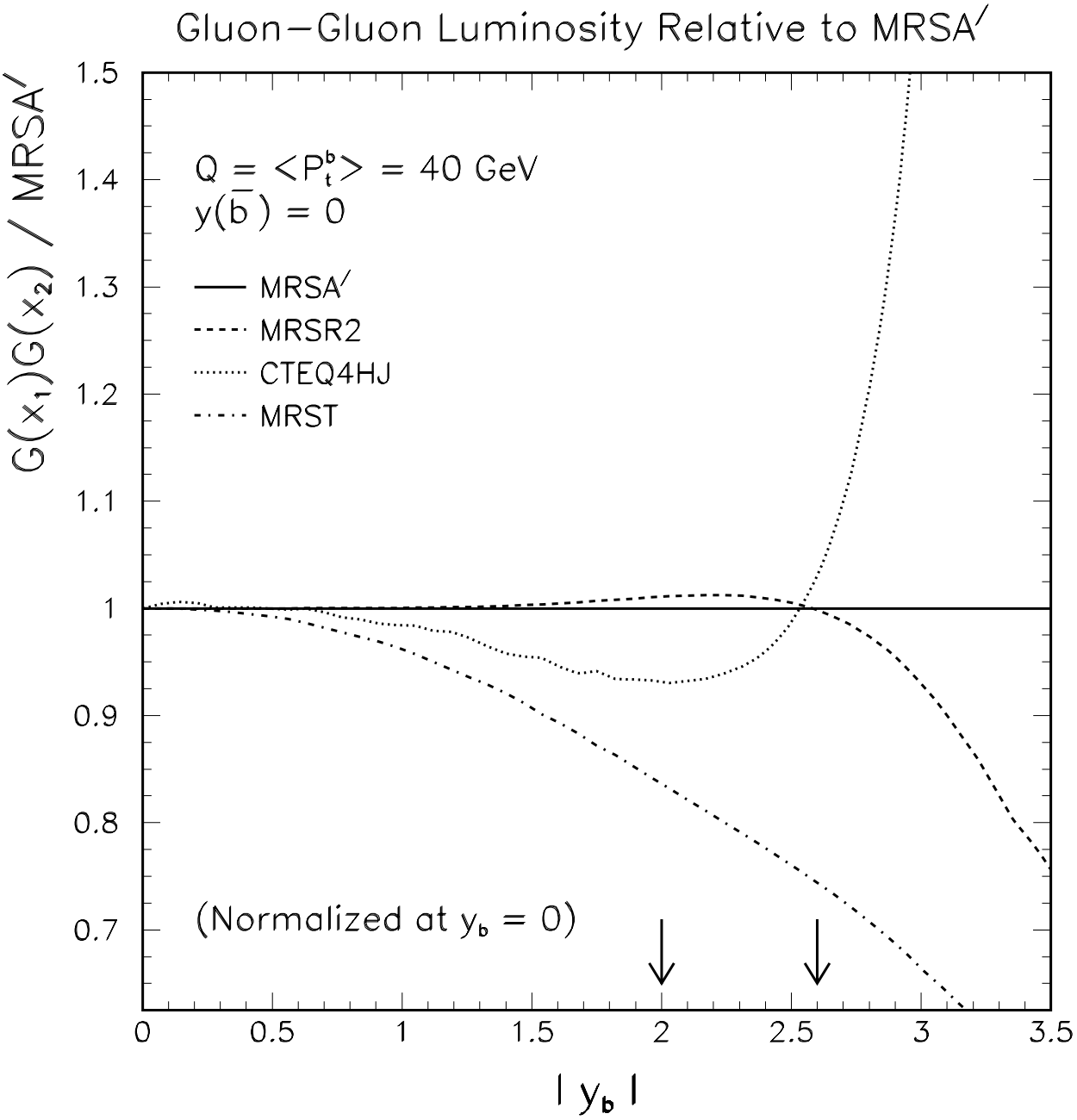

FIG. 18. Comparison of the gluon-gluon luminosity for MRSR2, CTEQ4HJ, and MRST PDFs, relative to MRSA′, as a function of $|y_b|$. Here we set $y_{\bar{b}} = 0$ and $Q = 40\,\mathrm{GeV}$. The curves are divided by MRSA′ and normalized to unity at $y_b = 0$. Arrows indicate the approximate region covered by our measurement.

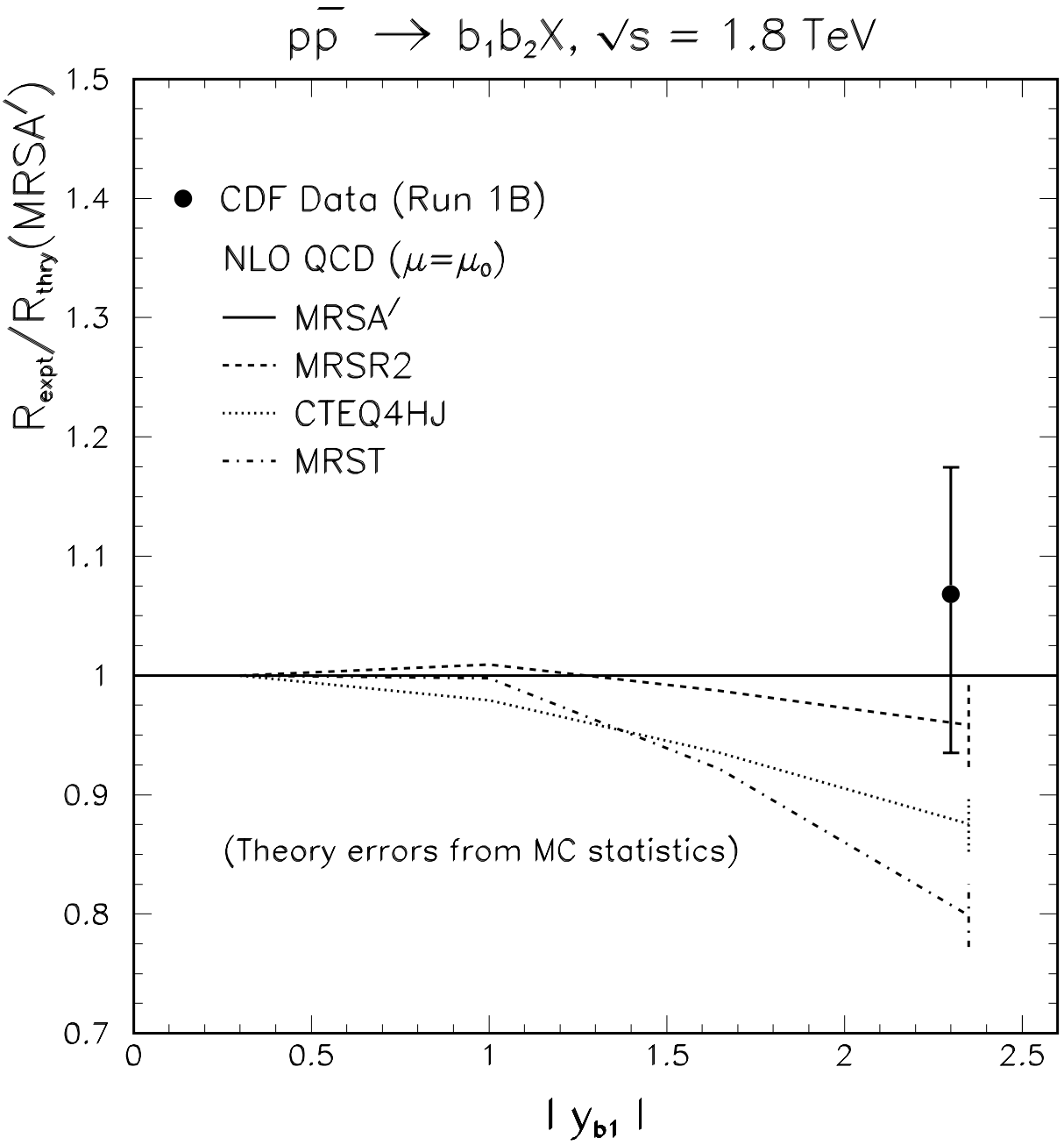

FIG. 19. Comparison of the ratio $R = \sigma(|y_{b_1}|)/\sigma(|y_{b_1}| < 0.6)$ between data and theory using MRSA′ parton distribution functions. Theory curves for MRSR2, CTEQ4HJ, and MRST are divided by MRSA′ and normalized to unity in the first bin. Theory error bars are the statistical uncertainty from Monte Carlo integration, while the data error is combined statistical and systematic.